



저작자표시-비영리-변경금지 2.0 대한민국

이용자는 아래의 조건을 따르는 경우에 한하여 자유롭게

- 이 저작물을 복제, 배포, 전송, 전시, 공연 및 방송할 수 있습니다.

다음과 같은 조건을 따라야 합니다:



저작자표시. 귀하는 원저작자를 표시하여야 합니다.



비영리. 귀하는 이 저작물을 영리 목적으로 이용할 수 없습니다.



변경금지. 귀하는 이 저작물을 개작, 변형 또는 가공할 수 없습니다.

- 귀하는, 이 저작물의 재이용이나 배포의 경우, 이 저작물에 적용된 이용허락조건을 명확하게 나타내어야 합니다.
- 저작권자로부터 별도의 허가를 받으면 이러한 조건들은 적용되지 않습니다.

저작권법에 따른 이용자의 권리는 위의 내용에 의하여 영향을 받지 않습니다.

이것은 [이용허락규약\(Legal Code\)](#)을 이해하기 쉽게 요약한 것입니다.

[Disclaimer](#)

이학박사학위논문

**The effect of oxygen functional  
groups on the electrical transport of  
multi-layered graphene oxide**

다겹산화그래핀의 산소반응기에 따른  
전기적 특성 연구

2015 년 2 월

서울대학교 대학원

나노융합학과 나노융합전공

백 승 재

# The effect of oxygen functional groups on the electrical transport of multi-layered graphene oxide

다결산화그래핀의 산소반응기에 따른  
전기적 특성 연구

지도교수 박 영 우

이 논문을 백승재 이학박사학위논문으로 제출함

2014 년 10 월

서울대학교 대학원  
나노융합학과 나노융합전공  
백 승 재

백승재의 이학박사학위논문을 인준함

2014 년 12 월

위 원 장           홍 승 훈           (인)

부위원장           박 영 우           (인)

위 원           박 원 철           (인)

위 원           이 탁 희           (인)

위 원           주 진 수           (인)

# **The effect of oxygen functional groups on the electrical transport of multi-layered graphene oxide**

*Baek Seungjae*

Supervised by

**Professor Park Yungwoo**

A Dissertation Submitted to the Faculty of Seoul National University in Partial Fulfillment of the Requirements for the Degree of Doctor of Philosophy

February 2015

*Department of Nano Science and Technology*

*Graduate School*

*Seoul National University*

# **Abstract**

## **The effect of oxygen functional groups on the electrical transport of multi-layered graphene oxide**

*Baek Seungjae*

**Department of Nano Science and Technology**

**The Graduate School**

**Seoul National University**

Graphene oxide (GO) has emerged as one of the active research fields as well as graphene. In early days, GO had been focused on obtaining good quality graphene. Nowadays, however, GO itself has been much attention due to various oxygen functional groups which can provide a facile method for hybrid structure, and applicability for energy device electrode by reduction to electrical conduction. Especially, Pd-doped GO is expected for hydrogen fuel cell electrode by providing large surface area and trap sites for well dispersed Pd nanoparticles. Although many conduction mechanism of GO already

reported, a comprehensive description on electrical conduction of multi-layered GO (MGO) was not enough. In this thesis, the electrical conduction mechanism of MGO and Pd-decorated MGO (PdGO) are investigated as a function of annealing temperature and H<sub>2</sub> gas pressure.

To investigate the electronic transport mechanisms in MGO, the temperature-dependent electrical conductivity ( $\sigma(T)$ ) has been measured as a function of annealing temperature ( $T_a$ ). An individual MGO flake is gradually reduced as the thermal annealing temperatures  $T_a$  increases from 88 to 300 °C, reduction process of MGO flake upon heating is confirmed by X-ray photoelectron spectroscopy at each annealing stage. As  $T_a$  increases,  $\sigma(T)$  of the MGO increases. The  $\sigma(T)$  is well interpreted by variable-range hopping in disordered regions in series with activated conduction across small barriers. The charge localized states are formed for hopping with the oxygen functional groups in GO, and the small activation barriers with the domain boundaries between the clustered oxygen functional groups and graphitic region. Both the hopping and activation barrier resistances decrease systematically as the  $T_a$  increases.

Afterwards, MGO and PdGO are electrically evaluated for adsorptive hydrogen pressure at room temperature. PdGO is made by Suzuki-Miyaura coupling reaction using the MGO and Pd acetate, and dispersed Pd nanoparticles are confirmed by high resolution TEM. A pressure-dependent

electrical conductance of MGO and PdGO has been measured in situ during hydrogen gas exposure (up to 20 bar) and release processes. As H<sub>2</sub> pressure increases, the electrical conductance of MGO is increases while that of PdGO is decreased. Using atomic force microscopy, X-ray photoelectron spectroscopy, and Fourier transform-infrared spectroscopy analysis, it was found that MGO reduction due to H<sub>2</sub> accounts for the increase in electrical conductance of the MGO. For PdGO, an increase of OH groups was observed, which shows that PdGO was oxidized when exposed to high H<sub>2</sub> pressure. The PdGO oxidation can be explained by a hydrogen spillover effect resulting in the decrease of electrical conductance.

**Key words** : Multi-layered graphene oxide, electrical property, Pd decoration, hydrogen dissociation, X-ray photoelectron spectroscopy, oxygen functional group.

**Student Number** : 2009-30729

# Contents

<b>Abstract</b> .....	<b>i</b>
-----------------------	----------

## **1. Introduction**

1.1. Brief review of graphene .....	1
1.2. Overview of graphene oxide .....	4
1.3. Characterization of graphene oxide	
1.3.1. XPS .....	9
1.3.2. FTIR .....	11
1.3.3. HRTEM .....	13

## **2. Charge transport mechanism**

2.1. Schottky emission .....	18
2.2. Fowler-Nordheim tunneling .....	20
2.3. Poole-Frenkel conduction .....	22
2.4. Hopping conduction .....	24

### **3. The effect of oxygen functional groups on the electrical transport behavior of a single piece multi-layered graphene oxide**

3.1. Introduction .....	29
3.2. Experimental	
3.2.1. Device fabrication .....	31
3.2.2. Electrical measurement .....	32
3.3. Results and discussion	
3.3.1. Thermal reduction .....	33
3.3.2. XPS spectra .....	36
3.3.3. Temperature-dependent conductivity of MGO .....	38
3.3.4. Temperature-dependent conductivity of FGO .....	46
3.4. Conclusion .....	49

### **4. Electrical Conduction of Palladium-decorated Multi-layered Graphene Oxide Effected by Hydrogen Dissociation**

4.1. Introduction .....	54
-------------------------	----

4.2. Experimental	
4.2.1. MGO and PdGO sheets fabrication .....	57
4.2.2. Device preparation .....	58
4.2.3. Electrical measurement .....	59
4.3. Results and discussion	
4.3.1. Electrical conductance of pristine MGO at high Pressure H <sub>2</sub> gas .....	60
4.3.2. XPS spectra of pristine MGO .....	62
4.3.3. Electrical conductance of PdGO at high Pressure H <sub>2</sub> gas .....	64
4.3.4. XPS spectra of Pd 3d of PdGO .....	66
4.3.5. FTIR spectra of PdGO .....	69
4.4. Conclusion .....	72
<b>5. Conclusion .....</b>	<b>77</b>

# List of Figures

1.1. rGO synthesis protocol for chemically assisted exfoliation of graphite based on the Hummers oxidation and subsequent sonication .....	5
1.2. Proposed structure of graphite oxide .....	6
1.3. The basic principle of XPS. 1) Excitation and emission of a photoelectron by radiation. 2) The hole is filled by an electron of a higher level and the released energy leads to the emission of an Auger electron .....	9
1.4. Schematic diagram of Michelson interferometer, configured for FTIR . .....	11
1.5. Ray diagram for a transmission electron microscope in image mode. In diffraction mode, another intermediate lens is inserted to image on the screen the diffraction pattern of the back focal plane .....	13
2.1. Schematic energy band diagram of Schottky emission in metal-insulator-semiconductor structure .....	19
2.2. Schematic energy band diagram of Fowler-Nordheim tunneling in metal-insulator-semiconductor structure .....	21
2.3. Schematic energy band diagram of Poole-Frenkel conduction in metal-	

insulator-semiconductor structure .....	23
2.4. Illustration of variable range hopping. The hopping length changes with the temperature .....	26
3.1. HRTEM image of MGO (a) before annealing (pristine), and (b) after annealing process at 400 °C .....	35
3.2. (a) Thermogravimetric profile of the MGO (Green line). (b) The thickness variation of MGO as a function of $T_a$ obtained from the AFM study .....	37
3.3. The variation of the amount of carbon and oxygen groups as $T_a$ increases .....	38
3.4. XPS spectra of the MGO at each annealing temperature .....	39
3.5. Schottky barrier limited charge transport fitting (plot) of each $T_a$ ....	41
3.6. (a) Temperature dependence of normalized $\sigma$ as a function of $T_a$ (b) Three dimensional VRH fitting .....	43
3.7. Three dimensional VRH with an added resistivity fitting .....	45
3.8. Schematic illustration of the combination model of VRH and activated conduction in series to demonstrate the overall conduction behavior .....	47

3.9. (a) Thickness variation of FGO as a function of Ta obtained from the AFM study. (b) Gate voltage-dependent $\sigma$ of the sample annealed at two different $T_a$ .....	49
3.10. (a) Electron and hole mobilities are shown by taking the slope in $\sigma - V_G$ curve. (b) Three dimensional VRH with an added resistivity fitting .....	50
4.1. (a) The AFM image of the MGO. (b) The $G$ of MGO during hydrogen exposure and release .....	63
4.2. C 1s XPS spectra of MGO before (a) and after (b) hydrogen exposure. (c) To compare the C 1s spectra of before and after H <sub>2</sub> exposure, the peaks are plotted simultaneously ((a) and (b)). (d) The amount of carbon species are evaluated from area weights in XPS spectra .....	65
4.3. (a) A transmission electron microscopy image shows that the MGO surface is decorated by Pd nanoparticles. (b) The $G$ of PdGO during hydrogen exposure and release .....	67
4.4. The XPS spectra for Pd 3d of the PdGO (a) before and (b) after H <sub>2</sub> exposure. (c) and (d) show XPS spectra of PdGO for C 1s before and after H <sub>2</sub> exposure .....	69
4.5. FTIR spectra of PdGO before and after H <sub>2</sub> exposure .....	72

# List of Table

1. Summary of the fitting parameters for our series VRH and activated model  
Eq. (2) for conduction in MGO for different annealing temperatures  $T_a$  ..45

# Chapter 1

## Introduction

### 1.1. Brief review of graphene

Graphene is a one-atom-thick planar sheet (0.34 nm) of two-dimensional honeycomb lattice of carbon. The carbon atoms of one sub-lattice are at the center of the triangles defined by the other with a carbon-to-carbon inter-atomic length of 0.142 nm. The unit cell comprises two carbon atoms and is invariant under a rotation of  $120^\circ$  around any atom. It is the basic building block of all the “graphitic” materials such as fullerene, carbon nanotube, and graphite. The emergence of graphene has recently opened up an exciting new field in the science and technology of two-dimensional nanomaterials with continuously growing academic and technological interest. Although the concept of graphene has been around since the 1940s, it was initially thought to be too thermodynamically unstable to exist under ambient conditions [1]. Graphene was first noticed on the platinum (100) surface in 1968 [2]. However, exfoliation of graphite into individual graphene

sheets remained a puzzle until 2004, when isolated graphene using the simple Scotch tape method [3] was reported. The subsequent discoveries of its unusual properties [4, 5] have led to tremendous interest among scientific researchers.

Graphene has a large theoretical specific surface area ( $2630 \text{ m}^2\text{g}^{-1}$ ), high intrinsic mobility ( $200,000 \text{ cm}^2\text{v}^{-1}\text{s}^{-1}$ ), [6, 7] high Young's modulus ( $\sim 1.0 \text{ TPa}$ ) [8] and thermal conductivity ( $\sim 5000 \text{ Wm}^{-1}\text{K}^{-1}$ ), [9] and its optical transmittance ( $\sim 97.7 \%$ ) [10] and good electrical conductivity merit attention for application such as for transparent conductive electrodes [11]. Importantly, these attractive properties have triggered huge interest from different research fields concerned with biomedicine, sensors, catalyst, transparent electrodes, energy conversion/storage and environmental pollution remediation. Moreover, fascinating transport phenomena such as the quantum Hall effect [12] and ambipolar electric field effect [13] are attracted for device physicists. The zero bandgap characteristic of graphene allows both electron and hole transport through ambipolar electric field effect. A carrier concentration is reached up to  $10^{13} \text{ cm}^{-2}$  and charge carriers can travel with extremely high mobility (for suspended samples,  $\sim 200,000 \text{ cm}^2\text{V}^{-1}\text{s}^{-1}$  at room temperature) because of their massless nature in the linear E-k dispersion at low energy. The high quality of graphene implies a low density of defects and graphene behaves like a metal. Moreover, transparent graphene films are considered as

a replacement material for indium tin oxide (ITO). These remarkable properties enable us to make graphene useful for device applications.

For a long time, graphene was considered thermodynamically unstable. Since graphene was discovered by mechanical exfoliation method in 2004, several methods - epitaxial growth, chemical vapor deposition (CVD), reduction of graphene oxide (GO) - have been successfully established for high quality graphene preparation. However, some of excellent characteristics have been achieved only for the mechanically exfoliated graphene sheet. Although these preparation methods are improving, equivalent characteristics have not been observed yet. Because defects, chemical impurities, and structural imperfections play a role to induce the decrease of the graphene quality. In addition, these different methods also produce graphene with different size, shape, and chemical composition. A high quality pristine graphene sheet obtained mechanical exfoliation is a fascinating system for condensed-matter physics and has allowed physicists to reveal the fundamental properties. However, it is insufficient to make large scale graphene-based materials for bulk production. If we divide into two preparation categories, these are bottom-up, and top-down approaches. The bottom-up approach is making the graphene sheets from simple carbon molecules. On the other hand, top-down approach is extracting layers from graphite. Regarding for mass production and low cost, the top-down approach

by reduction of graphene oxide is very convenient method. Therefore, oxidation and reduction of graphite is important research field.

## **1.2. Overview of graphene oxide**

Previously mentioned, one of the materials that played a prominent role in the development of graphene and its related materials is GO. This can be considered as a precursor for graphene synthesis. Actually GO is not a naturally occurring material. GO consists of a single-layer of graphite oxide and is usually produced by the chemical treatment of graphite through oxidation, with subsequent dispersion and exfoliation in water or suitable organic solvents. The synthesis of graphite oxide was first reported in the year of 1860 [14]. In 1958, Hummers and Offeman reported a new method that using potassium permanganate as oxidant in a mixture of sulphuric acid and sodium nitrate [15]. Nowadays, the Hummers method has been received and adopted by many researchers. GO is very similar to graphene related in carbon nanomaterials and, in their pristine, isolated forms etc. However, the properties of graphene and GO are very different. While graphene is composed of only  $sp^2$ -hybridized carbon atoms, GO has a carbon structure that is interrupted by oxygen functional groups. GO is also water soluble with low electronic conductivity. The excellent solubility of GO in aqueous

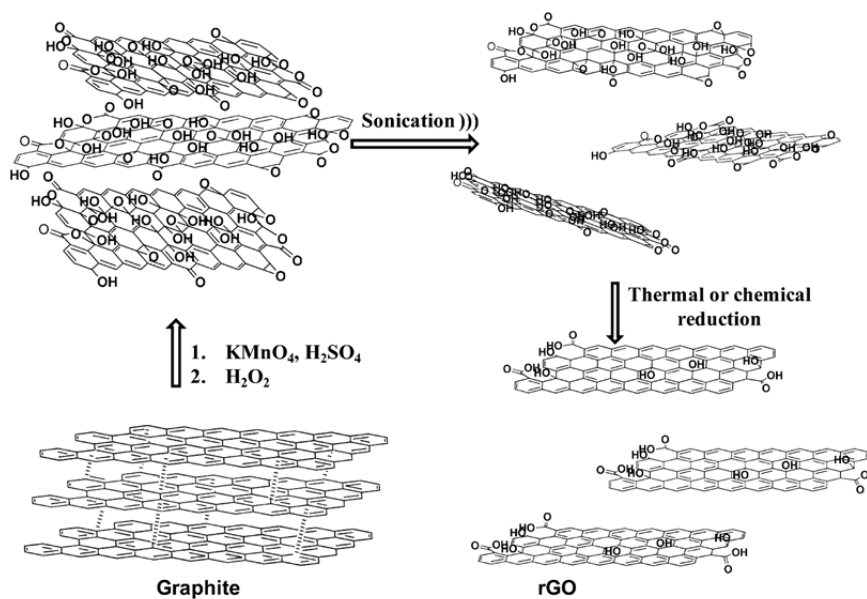
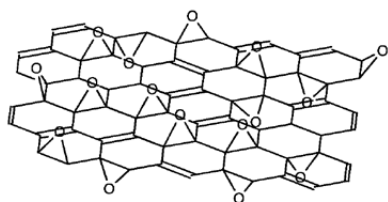
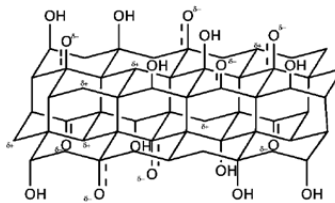


Fig. 1.1. rGO synthesis protocol for chemically assisted exfoliation of graphite based on the Hummers oxidation and subsequent sonication [22].

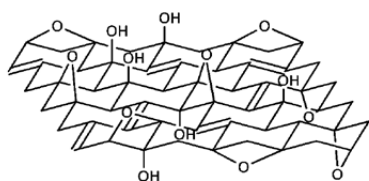
solution is primarily due to its rich oxygen-containing and hydrophilic groups, such as hydroxyl, epoxide, carboxyl and carbonyl. By using chemically or thermally reduction, most of the oxygen-containing groups, in particular the hydroxyl(-OH), epoxide(C-O-C) and carboxyl(O=C-O), will be (partially or totally) removed. Hence, GO will then be converted to good conductor: reduced GO (rGO). The rGO can restore the conductivity but decreases its solubility in water and other organic solvents. The decline in solubility of rGO may limit its applications. However, the presence of oxygen functional groups of GO can also provide potential advantages for other applications.



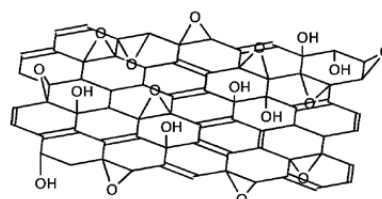
**Hofmann**



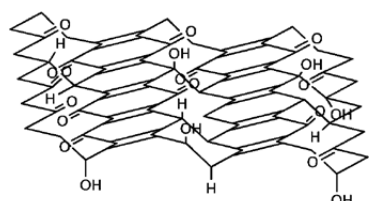
**Nakajima-Matsuo**



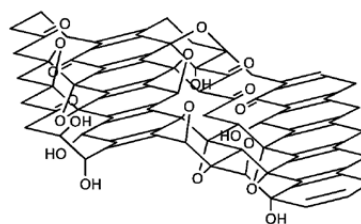
**Ruess**



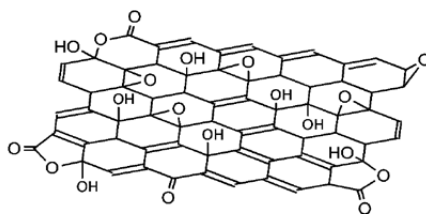
**Lorf-Klinowski**



**Scholz-Boehm**



**Dékány**



**Ajayan**

Fig. 1.2. Proposed structure of graphite oxide [20].

Understanding the structure of GO is important for chemical modifications. Its composition and structure of GO has been the subject of debate for many years due to its nonstoichiometric composition and the strong hygroscopicity of dehydrated graphite oxide [16]. Graphite oxide consists of layered structure of GO sheets and carbon to oxygen ratio is about 1.5 to 2.5. The inter-layer distance between the GO sheets varied from 0.6 to 1.2 nm due to the difference of the amount of oxygen functional groups, water molecules, and other impurities. The oxygen functional groups between graphite layers are interesting starting materials to obtain colloidal dispersions of single layer graphene sheets. By simple sonication, graphite oxide can be exfoliated to colloidal suspensions of graphene sheets. There are several models for preparing GO. Indicating the Staudenmaier [13], Brodie [14], Hofmann [17], Hummers [18], and Tour [19] methods at least seven different approaches for synthesizing GO have been described [20]. The structures of GO's constituent oxygen functionality can vary as a function of the graphite precursor, oxidation conditions, and process treatments. As a result, identifying and quantifying the various functional groups present in GO has proved to be remarkably challenging. The most widely accepted structural model of GO is the Lerf-Klinowski model. In this model, hydroxyl and epoxide groups are proposed to decorate the basal plane, graphene-like regions, while carboxylic acids or carboxylates, depending on the pH of the solution, are present on the

edges of the sheets [19]. An observation of graphite oxide using high-resolution transmission electron microscopy (TEM) has indicated the presence of such features on the graphite oxide sheets, in support of the Lerf-Klinowski model [21].

In order to convert from GO to graphene, reduction process such as thermal, chemical, and electrochemical methods have to be applied. During the reduction process, oxygen functional groups on (in) graphite/graphene oxide can be removed. However, the use of hydrazine vapor for chemical reduction is toxic and potentially explosive. Therefore, several other reductants have been explored. Thermal reduction process in vacuum or in Ar atmosphere at high temperature have been also carried out. In this thesis, a thermal annealing was carried out at a temperature of 300°C in an Ar atmosphere. In addition, three different methods would induce the different performances in electronic, physical, and structural properties. Even though there are much defects exist in reduced GO (rGO), these are suitable for applications.

## 1.3. Characterization of graphene oxide

### 1.3.1. X-ray photoelectron spectroscopy (XPS)

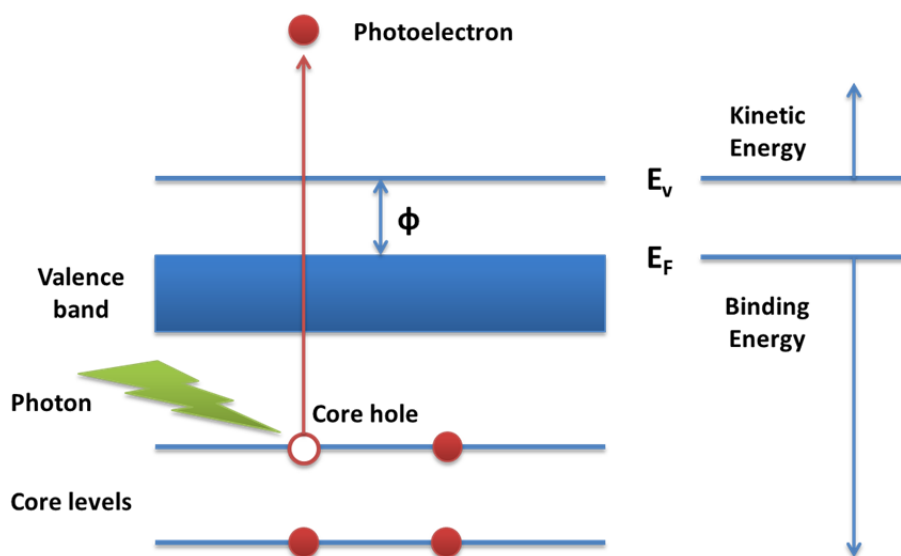


Fig. 1.3. The basic principle of XPS. 1) Excitation and emission of a photoelectron by radiation. 2) The hole is filled by an electron of a higher level and the released energy leads to the emission of an Auger electron.

X-ray photoelectron spectroscopy (XPS) is a surface-sensitive quantitative spectroscopic technique that measures the elemental composition based on the photoelectric effect. The technique was first known by the acronym ESCA (Electron Spectroscopy for Chemical Analysis). XPS works by irradiating a sample material with X-ray. This X-ray excites the electrons

of the sample atoms and if their binding energy is lower than the X-ray energy, they will be emitted from the parent atom as a photoelectron. Only the photoelectron at the extreme outer surface (1-10 nm) can escape the sample surface, making this a surface analysis technique. Binding energy (BE) represents strength of interaction between electron ( $n, l, m, s$ ) and nuclear charge. The relationship governing the interaction of a photon with a core level is:

$$KE = h\nu - BE - e\phi$$

Where KE is kinetic energy of ejected photoelectron,  $h\nu$  is characteristic energy of X-ray photon, BE is binding energy of the atomic orbital from which the electron originates, and  $e\phi$  is spectrometer work function. Identification of the elements in the sample can be made directly from the kinetic energies of these ejected photoelectrons. The relative concentrations of elements can be determined from the photoelectron intensities. An important advantage of XPS is its ability to obtain information on chemical states from the variations in binding energies, or chemical shifts, of the photoelectron lines.

### 1.3.2. Fourier transform infrared spectroscopy (FT-IR)

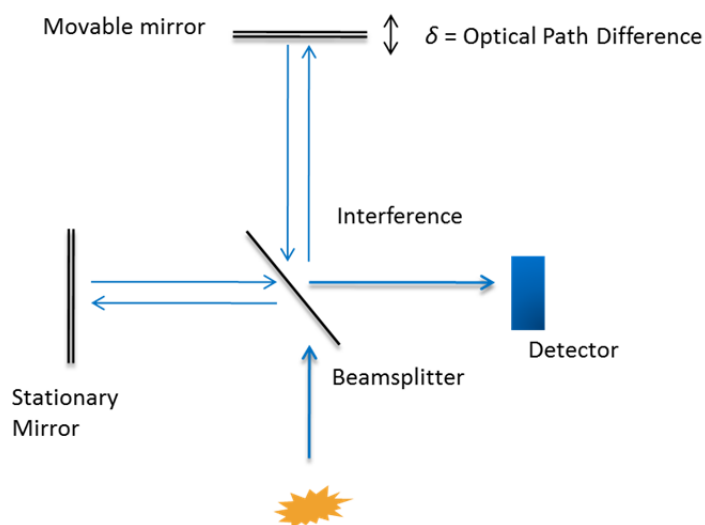


Fig. 1.4. Infrared light emitted from a source is directed into an interferometer, which modulates the light. After the interferometer the light passes through the sample compartment (and also the sample) and is then focused onto the detector. The moving mirror oscillates at a constant velocity, timed using the laser frequency. The two beams are reflected from the mirrors and are recombined at the beamsplitter. The movement of the mirror thus generates an interference pattern during the motion. The signal measured by the detector is called the interferogram.

FTIR stands for Fourier Transform Infrared Spectroscopy is highly sensitive and quick method to achieve high quality spectrum. This spectroscopy gives better signal to noise ratio compared to the dispersive instrument. In infrared spectroscopy, IR radiation is passed through a sample.

Some of the infrared radiation is absorbed by the sample and some of it is transmitted. The resulting spectrum represents the molecular absorption and transmission, creating a molecular fingerprint of the sample. From the FT-IR analysis, we can identify unknown materials, determine the quality of sample, and determine the amount of component in mixture.

The advantages of this technique are as follows. Solid, gases, and liquid can be analysed with non-destructively and simultaneously with FT-IR. It is a major advantage of infrared spectroscopy that the samples being viewed don't require any sort of special preparation. It generally completes a scans with 1 to 2 second. Also it shows high resolution, and sensitivity is very high. These advantages make FT-IR extremely accurate and reproducible. Therefore, it is very reliable method to identify the composition of any sample.

Many functional groups absorb infrared radiation at about the same wavenumber, regardless of the structure of the rest of the molecule. Typically IR spectra show features at  $\sim 1060\text{ cm}^{-1}$  (C-O),  $\sim 1228\text{ cm}^{-1}$  (-OH; in alcohol),  $\sim 1395\text{ cm}^{-1}$  (C-O; in carboxyl),  $\sim 1627\text{ cm}^{-1}$  (C=C), and  $\sim 1720\text{ cm}^{-1}$  (C=O). This makes these bands reference markers for the presence of functional groups in a sample. These types of infrared bands are called group frequencies because they tell us about the presence or absence of specific functional groups in a sample.

### 1.3.3. High resolution transmission electron microscopy (HR-TEM)

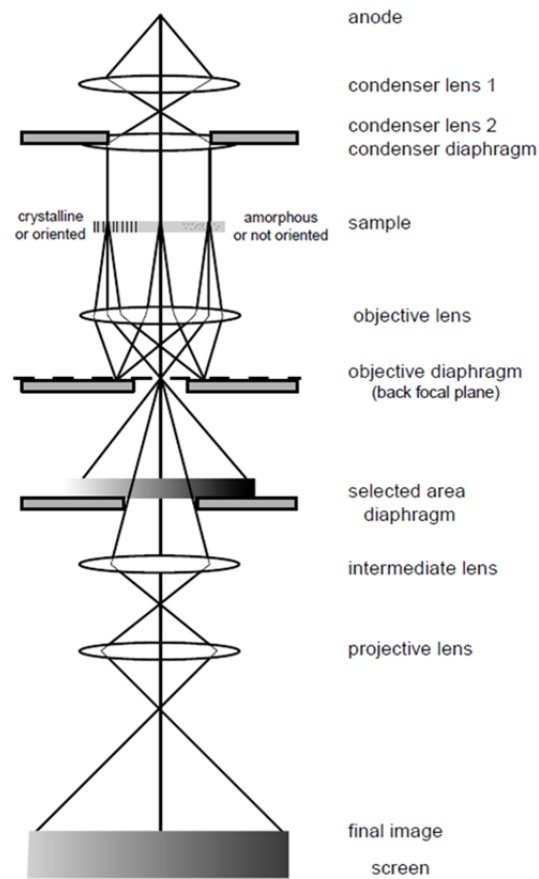


Fig. 1.5. Ray diagram for a transmission electron microscope in image mode. In diffraction mode, another intermediate lens is inserted to image on the screen the diffraction pattern of the back focal plane. (*Illustration from wikipedia*)

The high-resolution transmission electron microscopy (HRTEM) uses both the scattered and transmitted beams. The beams create an

interference images that provides morphological, compositional and crystallographic information. The HRTEM is composed of an illumination system, condenser lens system, an objective lens system, magnification system, and the data recording system. A set of condenser lens that focus the beam on the sample and an objective lens collects all the electrons after interacting with the sample and form image of the sample, and determines the limit of image resolution. The speed of electrons is directly related with the electron wavelength and determines the image resolution. The image is formed by the interference of the diffracted beams with the direct beam (phase contrast). If the point resolution of the microscope is sufficiently high and a suitable crystalline sample oriented along a zone axis, then HRTEM images are obtained. In many cases, the atomic structure of a specimen can directly be investigated by HRTEM.

The HRTEM has been extensively and successfully used for analyzing crystal structures and lattice imperfections in various kinds of advanced materials on an atomic resolution scale. It allows the imaging of the structure of a sample at an atomic level such as surface structures, interface, dissociation, defects, etc. (resolution  $< 1$  nm). A main advantageous characteristic of a transmission electron microscope is the possibility to obtain information in real space (imaging mode) and reciprocal space (diffraction mode) almost simultaneously.

# Bibliography

- [1] Daniel R. Dreyer, Rodney S. Ruoff, and Christopher W. Bielawski, *Angew Chem. Int. Ed.* **49**, 9336 (2010)
- [2] A. E. Morgan and G. A. Somorjai, *Surf. Sci.* **12**, 405 (1968)
- [3] K. S. Novoselov, A. K. Geim, S. V. Morozov, D. Jiang, Y. Zhang, S. V. Dubonos, I. V. Grigorieva, A. A. Firsov, *Science* **306**, 666 (2004)
- [4] K. S. Novoselov, Z. Jiang, Y. Zhang, S. V. Morozov, H. L. Stormer, U. Zeitler, J. C. Maan, G. S. Boebinger, P. Kim, A. K. Geim, *Science* **315**, 1379 (2007)
- [5] Yuanbo Zhang, Yan-Wen Tan, Horst L. Stormer, and Philip Kim, *Nature* **438**, 201 (2005)
- [6] K.I. Bolotin, K.J. Sikes, Z. Jiang, d, M. Klima, G. Fudenberg, J. Hone, P. Kim, and H.L. Stormer, *Solid State Commun.* **146**, 351 (2008)
- [7] S. V. Morozov, K. S. Novoselov, M. I. Katsnelson, F. Schedin, D. C. Elias, J. A. Jaszczak, and A. K. Geim, *Phys. Rev. Lett.* **100**, 016602 (2008)
- [8] Changgu Lee, Xiaoding Wei, Jeffrey W. Kysar, and James Hone, *Science* **321**, 385 (2008)

- [9] Alexander A. Balandin, Suchismita Ghosh, Wenzhong Bao, Irene Calizo, Desalegne Teweldebrhan, Feng Miao, and Chun Ning Lau, *Nano Lett.* **8**, 902 (2008)
- [10] Weiwei Cai, Yanwu Zhu, Xuesong Li, Richard D. Piner, and Rodney S. Ruoff, *Appl. Phys. Lett.* **95**, 123115 (2009)
- [11] Xuesong Li, Yanwu Zhu, Weiwei Cai, Mark Borysiak, Boyang Han, David Chen, Richard D. Piner, Luigi Colombo, and Rodney S. Ruoff, *Nano Lett.* **9**, 4359 (2009)
- [12] Sylvain Latil and Luc Henrard, *Phys. Rev. Lett.* **97**, 036803 (2006)
- [13] L. Staudenmaier, *Ber. Dtsch. Chem. Ges.* **31**, 1481 (1898)
- [14] B. C. Brodie, *Philos Trans R Soc (London) A* **149**, 249 (1859)
- [15] William S. Hummers Jr. and Richard E. Offeman, *J. Am. Chem. Soc.* **80**, 1339 (1958)
- [16] Da Chen, Hongbin Feng, and Jinghong Li, *Chemical Reviews* **112**, 6027-6053 (2012)
- [17] U. Hofmann and E. Konig, *Z. Anorg. Allg. Chem.* **234**, 311 (1937)
- [18] William S. Hummers Jr. and Richard E. Offeman, *J. Am. Chem. Soc.* **80**, 1339 (1958)

- [19] Daniel R. Dreyer, Alexander D. Todd, and Christopher W. Bielawski, *Chem. Soc. Rev.* **43**, 5288 (2014)
- [20] Chun Kiang Chua and Martin Pumera, *Chem Soc. Rev.* **43**, 291 (2014)
- [21] K. Erickson, R. Erni, Z. Lee, N. Alem, W. Gannett, and A. Zettl, *Adv. Mater.* **22**, 4467 (2010)
- [22] Sergio Navalon, Amarajothi Dhakshinamoorthy, Mercedes Alvaro, and Hermenegildo Garcia, *Chem. Rev.* **114**, 6179 (2014)

# Chapter 2

## Charge transport mechanism

Understanding the conduction mechanism in disordered materials such as GO, and organic molecular layer has attracted due to their potential applications. Especially the GO is extensively studied because it can be simply converted to graphene. The GO is nearly insulator, whereas graphene shows metallic behavior. The purpose of reducing of the GO is removing the oxygen functional groups. However, in the majority cases, reduced GO (rGO) has much defects, and oxygen functional groups in (on) the surface. Such oxygen functional groups affect the charge conduction. In this chapter, possible conduction mechanism will be described.

### 2.1. Schottky (Thermionic) emission

Schottky emission is a conduction mechanism that the electrons obtain enough energy provided by thermal activation, the electrons can overcome the barrier height at the contact region (metal-insulator interface). The minimum energy required for an electron to escape the surface of a

specific material, called the work function. A Schottky barrier refers to a metal-semiconductor contact having a large barrier height (i.e.  $\phi_B > k_B T$ ). The barrier height is defined as the potential difference between the Fermi energy of the metal and the band edge. In thermal equilibrium the Fermi levels on either side of the interface must be equal and therefore a net charge transfer will occur at the interface. The Schottky effect also occurs in electric fields  $E$  that are strong enough to neutralize the space charge at the surface.

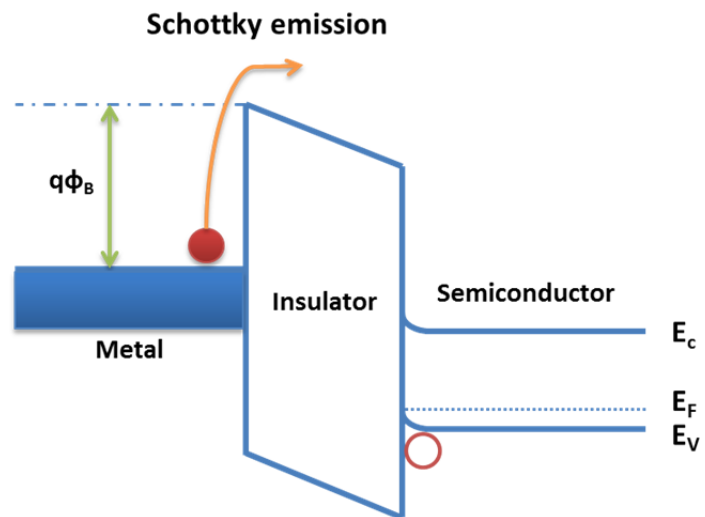


Fig. 2.1. Schematic energy band diagram of Schottky emission in metal-insulator-semiconductor structure.

The expression of Schottky emission is

$$J = A^* T^2 \exp \left[ \frac{-q(\Phi_B - \sqrt{qE / 4\pi\epsilon_r\epsilon_0})}{k_B T} \right]$$

$$(A^* = \frac{4\pi q k_B^2 m^*}{h^3} = \frac{120 m^*}{m_0})$$

where  $J$  is the current density,  $A^*$  is the effective Richardson constant,  $m_0$  is the free electron mass,  $m^*$  is the effective electron mass in dielectric,  $T$  is the absolute temperature,  $q$  is the electronic charge,  $q\phi_B$  is the Schottky barrier height,  $E$  is the electric field across the dielectric,  $k_B$  is Boltzmann's constant,  $h$  is Planck's constant,  $\epsilon_0$  is the permittivity in vacuum, and  $\epsilon_r$  is the optical dielectric constant.

## 2.2. Fowler-Nordheim tunneling

In quantum mechanics, the electron wave function will tunnel through energy barrier can be predicted. The probability of electrons existing at the other side of the energy barrier is not zero. When large positive voltage is applied to the metal, the right-hand side of the band diagram is lowered, and tunneling of electrons from the conduction band of the semiconductor into the conduction band of the insulator, through an approximately triangular barrier can occur, as shown in Fig. 2.2 (The energy band conditions for Fowler-

Nordheim tunneling, which is a special case of direct tunneling). The Fowler-Nordheim regime is significant for thicker dielectrics and sufficiently high electric fields.

The expression of Fowler-Nordheim tunneling is [1].

$$J = \frac{q^3 E^2}{8\pi h q \Phi_B} \exp \left[ \frac{-8\pi(2qm_T^*)^{1/2}}{3hE} \Phi_B^{3/2} \right]$$

where  $m_T^*$  is the tunneling effective mass in insulator. The assumption of this equation is well described in *ref* 1-3. These are (1) The electrons on the emitting electrode can be describe as a free Fermi gas (2) The dependence of

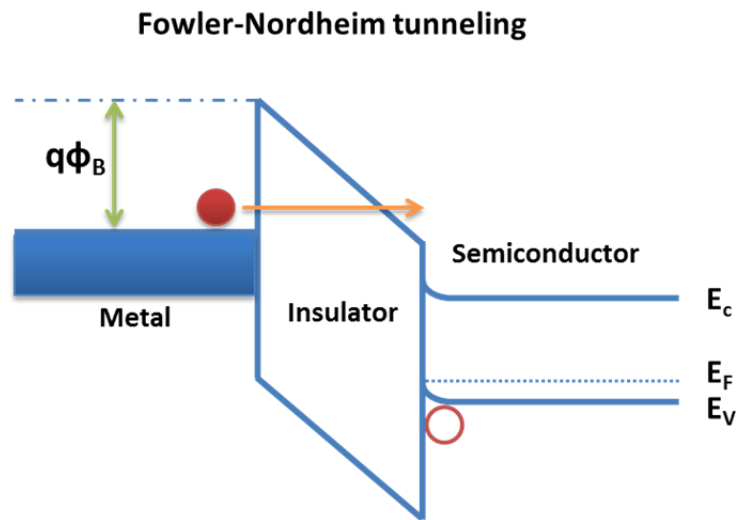


Fig. 2.2. Schematic energy band diagram of Fowler-Nordheim tunneling in metal-insulator-semiconductor structure.

carrier availability for tunneling with respect to temperature is not taken into account (3) The potential barrier has triangular shape and barrier lowering due to image forces is neglected (4) The effect of the insulator can be described by a single effective mass (5) The tunneling probability takes into account only the component of the electron momentum in the direction normal to the surface.

### **2.3. Poole-Frenkel conduction**

The Poole-Frenkel (PF) conduction mechanism is dominant in insulator (dielectric film) which has a large trap density and is thick enough to avoid tunneling process [4]. The Fowler-Nordheim tunneling implies that carriers are free to move through the insulator. However, PF conduction is a kind of trap assisted transport mechanism. The structural defects cause additional energy states close to the band edge, called traps. These traps restrict the current flow because of a capture and emission process, thereby becoming the dominant current mechanism. In other words, wave functions are localized, decaying exponentially away from trap sites (potential wells). Conduction is due to hopping from localized site to localized site. Hopping can be thermally activated (though it can also be due to tunneling). Applying a large electric field can affect *thermal* hopping rates. Lowering of hopping

barriers in large electric field is called PF behavior.

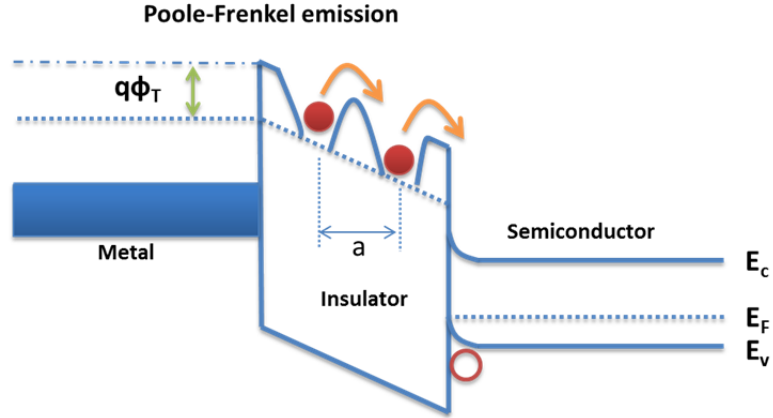


Fig. 2.3. Schematic energy band diagram of Poole-Frenkel conduction in metal-insulator-semiconductor structure.

The number of electrons which can participate in the PF conduction is considered to be identical to that of the traps in the film on the assumption that one trap donates one electron. And most of the traps are assumed to remain in electrically neutral states [5]. For a Coulomb attraction potential between electrons and traps, the current density due to the PF conduction is [6]

$$J = q\mu N_C E \exp \left[ \frac{-q(\phi_T - \sqrt{qE / \pi\epsilon_i\epsilon_0})}{k_B T} \right]$$

Where  $\mu$  is the electronic drift mobility,  $N_C$  is the density of states in the conduction band,  $q\phi_T$  is the trap energy level. This conduction mechanism is

based on thermal activation under an electric field, so it is often observed at high temperature and high electric field.

## **2.4. Hopping conduction**

After development of a transistor, it has been observed a break in the behavior of conductivity of Ge doped semiconductor at low temperatures. In 1956, Conwell [7] and Mott [8] suggested a model for a new process of conduction in which charge carriers conduct the electric current by thermally activated tunneling from an occupied site to an empty site. This process has been known as phonon assisted hopping and triggered a new theories (or model) such as Miller and Abrahams models developed in 1960 [9]. This model is most widely accepted theory of conduction mechanism. This model became the foundation of the variable range hopping (VRH) theory of Mott [10-12].

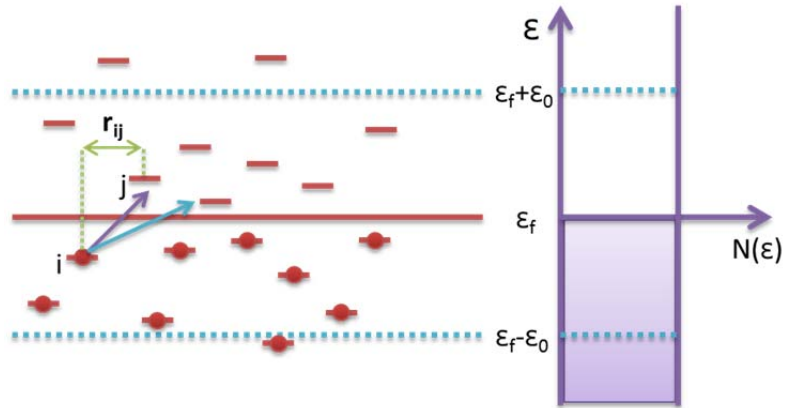


Fig. 2.4. Illustration of variable range hopping. The hopping length  $r_{ij}$  changes with the temperature.

The wave function of the localized states is proportional to  $\exp[-(2r/a)]$ , where  $a$  is the site distance and  $r$  is the hopping distance. The probability of hopping is described as a product of a tunneling term and a thermally activated term. Therefore, the probability of hopping between two localized sites is proportional to

$$P \sim \exp\left[-\frac{2r}{a} - \frac{W}{k_B T}\right] \quad (1)$$

For a hopping process through a distance  $r$ , the average hopping energy  $W$  is given as

$$\Delta W \propto \Delta \cdot \left(\frac{a}{r}\right)^3 \propto \frac{1}{g \cdot r^3} \quad (2)$$

Here,  $\Delta$  is the uniform barrier energy on each site and  $g$  is the density of state of the localized sites. In 3-dimension, the density of localized states  $g$  is given as

$$g = \frac{N}{V} = \frac{1}{\frac{4\pi a^3}{3}} \cdot N \quad (3)$$

$$a^3 = \frac{3}{4\pi \cdot g} \cdot N$$

where  $N$  is the total number of localized states. The maximum for the average hopping probability is obtained for an optimal value of  $r$ . In here, the hopping probability is rewritten as

$$P = \exp[f(r)]$$

$$\text{and } f(r) = -\frac{2r}{a} - \frac{A}{k_B T \cdot g r^3} \quad (4)$$

To obtain the maximum value of this quantity,

$$\frac{\partial f(r)}{\partial r} = -\frac{2}{a} + \frac{3}{k_B T \cdot g} \cdot r^{-4} = 0 \quad (5)$$

$$\therefore r^4 = \frac{3a}{2k_B T \cdot g} \quad (6)$$

This clearly shows that the hopping distance  $r$  increases at low temperature.

By substituting eq. (6) into eq. (4), the hopping probability in 3-dimension becomes

$$P \approx \exp \left[ -\left( \frac{T_0}{T} \right)^{\frac{1}{4}} \right] \quad (7)$$

The  $T_0$  is the hopping temperature typically in a range of  $T_0 \sim 10^5$  K. In general, for a system of dimension  $d$ , the hopping probability is written as

$$P \approx \exp \left[ -\left( \frac{T_0}{T} \right)^{\frac{1}{d+1}} \right] \quad (8)$$

# Bibliography

- [1] Lezlinger M, and Snow E. H. *J. Appl. Phys.* **40**, 278 (1969)
- [2] Weinberg Z. A. *J. Appl. Phys.* **53**, 5052 (1982),
- [3] Juan C. Ranuarez, M. J. Deen, and Chih-Hung Chen, *J. Microrel.* **46**, 1939 (2006)
- [4] J. Frenkel, *Phys. Rev.* **54**, 647 (1938)
- [5] Doo Seok Jeong and Cheol Seong Hwang, *J. Appl. Phys.* **98**, 113701 (2005)
- [6] Fu-Chien Chiu, *Adv. Mater. Sci. Eng.* **2014**, ID : 578168 (2014)
- [7] E. M. Conwell, *Phys. Rev.* **103**, 51 (1956)
- [8] N. F. Mott, *J. Phys.* **34**, 1356 (1956)
- [9] A. Miller, and E. Abrahams, *Phys. Rev.* **120**, 745 (1960)
- [10] N. F. Mott, *Phil. Mag.* **19**, 835 (1960)
- [11] N. F. Mott and E. A. Davis, *Phil. Mag.* **17**, 1269 (1968)
- [12] N. F. Mott and E. A. Davis, *Electronic process in non-crystalline materials* (Clarendon Press, Oxford (1979))

## **Chapter 3**

### **The effect of oxygen functional groups on the electrical transport behavior of a single piece multi-layered graphene oxide**

#### **3.1. Introduction**

Graphene has been researched extensively since it has exotic properties such as the anomalous quantum Hall effect caused by peculiar band structure and excellent electrical, mechanical, thermal, and optical properties [1-5]. However, the electronic structure of graphene must be controlled to apply in the electronics industry. Not only nanosized graphenes such as nano-ribbon [6], nano-flakes [7] and quantum dots but doped graphene [8-11] is considered as the potential components for nanoelectronic devices. Moreover, for a practical application of graphene, the mass production is important as well as electronic modification. Therefore, reduced graphene oxide (GO) has been regarded as a promising material for application.

GO is easily dispersed in water due to the oxygen functional groups (hydroxyl, epoxy, carbonyl, and carboxyl groups) that allow it to easily

manipulate the graphene. Multi-layered GO (MGO) is also known to have a layered structure with an interlayer distance that varies from 0.6 to 1.2 nm [12, 13]. Due to these properties, GO has been used as a building block for various applications in composites, transparent paper-like materials, mechanical actuators, nanorobots, molecular sensors, supercapacitors, and hydrogen storage materials [14-21]. Intrinsic properties, like the oxygen atom sites in GO and the oxygen concentration-dependence of the conductivity ( $\sigma$ ) have been investigated [22-33]. However, there is still an open issue regarding the charge transport mechanisms of GO. Various conduction mechanisms such as Mott variable range hopping (VRH) [26-29], Efros-Shklovskii (ES) VRH (the modified VRH model that considers the Coulomb gap) [30], Arrhenius (activated) behavior [31, 32], and fluctuation-induced tunneling (FIT) [33] conduction have been suggested. An Arrhenius (activated) behavior fits well in the high and low temperature regime, but not for the temperature range as a whole [32]. The VRH models, including the ES-VRH mechanism, have been proposed to explain the electrical conduction of reduced GO, because the oxygen functional groups of GO produce localized charge carriers. Both models focus on the oxygen functional groups in order to interpret the conduction mechanism of GO. The theoretical calculations suggested that the oxygen functional groups on the carbon atoms were formed as a clustered structure, much like the clustered hydrogen atoms on a carbon surface [34-36].

This indicates that the GO is composed of the carbon domains functionalized by oxygen groups and the graphitic region. The domain is distinguished from the graphitic region by a domain boundary, so the conduction mechanism in MGO can form a combination of two different mechanisms: one from the oxygen functional groups and the other from the domain boundary. Unlike an earlier study [27] that investigated GO films, we report the temperature-dependent conductivity ( $\sigma(T)$ ) of individual MGO flakes subject to different annealing conditions. We show that combining VRH and activated conduction in series is required to understand the overall conduction behavior of the reduced MGO.

## **3.2. Experimental**

### ***3.2.1. Device fabrication***

GO sheets were produced by utilizing the Hummers method [37] while the GO devices were prepared by drop casting, which is applicable for a wide range of substrates. The GO sheets were obtained via ultra-sonication in deionized water using a bath-type sonicator before the solution was centrifuged at 10,000 rpm for 5 minutes. Then, the supernatant was dropped onto the highly p-doped ( $\rho < 0.005 \text{ } \Omega\cdot\text{cm}$ ) silicon wafer covered by a thermally grown  $\text{SiO}_2$  layer (300 nm thickness). Before it was fully dried, the dropped solution was blown out with  $\text{N}_2$  gas to avoid a densely packed GO

layer. A conventional electron-beam lithography (VEGA MM5150 with 30 keV, TESCAN) and Ti/Au (5/50 nm) was deposited on top of the GO using the thermal evaporation system (MHS-1800, Muhan Vacuum) in order to define the electrode.

### ***3.2.2. Electrical measurement***

The devices were placed on a horizontal tube-type furnace (Ajeon Heating Industry) to reduce the GO. Before thermal annealing was conducted, we pumped out the chamber ( $< 10^{-2}$  Torr) to remove any remaining gas or water in the air. The flow rate of Ar gas was 100 sccm and thermal annealing was performed at 88, 158, 185, 215, 250, and 300 °C for 2 hrs.

From the thermogravimetric analysis (TGA), we observed GO decreasing in sheet mass. We then selected the annealing temperatures based on the inflection point of the curve in the TGA profile. The tapping mode AFM at 0.5 Hz confirmed the decrease in the GO sheet's height while the annealing temperature increased. XPS was also carried out to probe the components of the GO sheet, and the  $\sigma(T)$  was measured using a closed loop cryogenic system with a temperature controller (331 Temperature controller, Lakeshore). The current-voltage characteristics and  $\sigma(T)$  vs. gate voltage ( $V_G$ ) were measured with a semiconductor characterization system (SCS-4200, Keithley) at temperatures from 300 K to 60 K.

### 3.3. Results and discussion

#### 3.3.1. Thermal reduction

The thermal reduction process was done up to 300 °C. Because the Au electrode were melted down and their nanoparticles were deposited on GO when the annealing temperature was rased up to 1100 °C (even 400 °C), we could not measure the conductivity of the GO itself. The purpose of this study is the research of the conduction mechanism that is related to oxygen functional group. So,  $T_a = 300^{\circ}\text{C}$  is sufficient for this study.

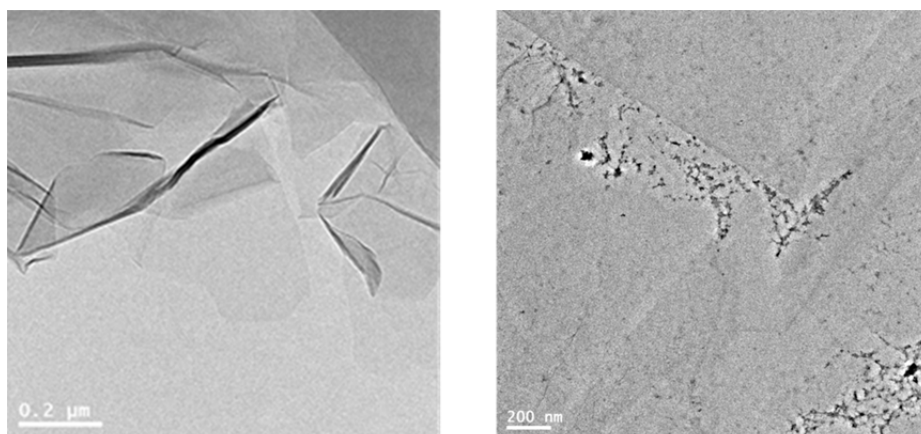


Fig. 3.1. HRTEM image of MGO (a) before annealing (pristine), and (b) after annealing process at 400 °C. The Au nanoparticles are melted down, and dispersed on the MGO surface.

The thermal annealing temperature,  $T_a$ , of GO was determined using thermogravimetric analysis (TGA) (Fig. 3.2(a)). We were able to find the GO weight loss in a temperature range from 20 °C to 185 °C, which was possible due to the trapped water evaporation and loosely bound functional groups. Further mass loss was found to occur between 185 °C and 250 °C and was attributed to the removal of tightly bound oxygen functional groups [38]. The TGA profile shows five different inflection points, defined as  $T_a$  ( $T_a = 88, 158, 185, 215, 250, \text{ and } 300 \text{ }^\circ\text{C}$ ). The thickness of the reduced MGO as a function of  $T_a$  was measured through atomic force microscopy (AFM) in Fig. 3.2(b), which showed that as the  $T_a$  increased, the thickness ( $t$ ) decreased from 30.1 nm (~34 layers of GO) to 19.3 nm.

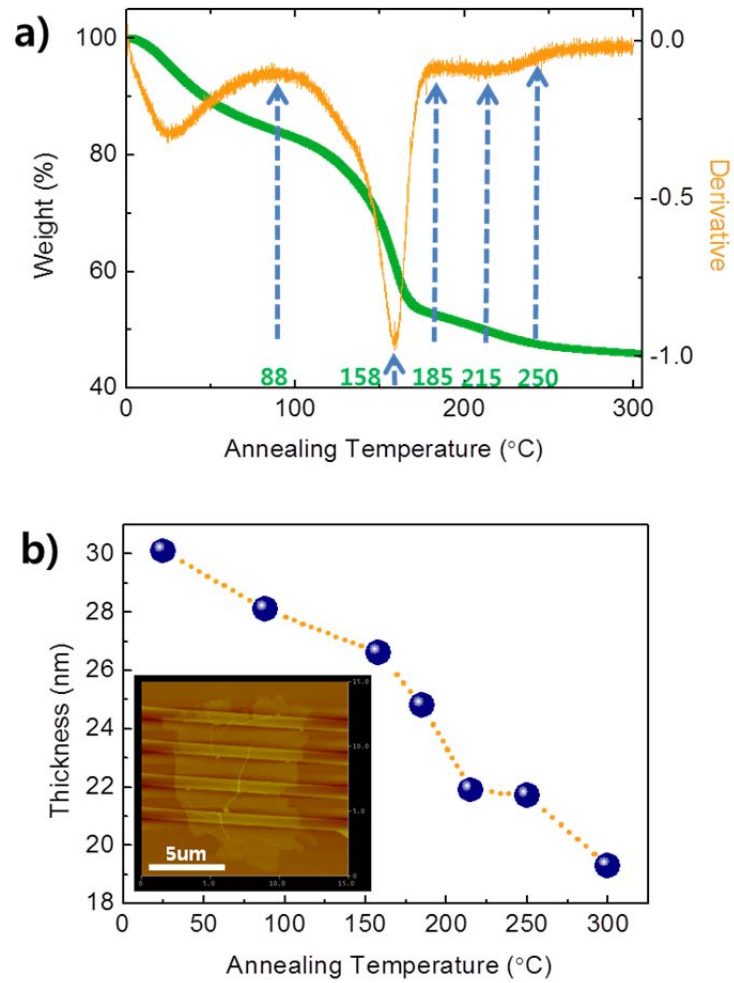


Fig. 3.2. (a) Thermogravimetric profile of the MGO (Green line). The orange line is the slope of the TGA curve while the blue dotted arrows are the inflection points of TGA. (b) The thickness variation of MGO as a function of  $T_a$  obtained from the AFM study. Inset shows the AFM image of the MGO

### 3.3.2. XPS spectra

The reduction of the (M)GO was also investigated with XPS (Fig. 2). The  $sp^2$  carbon (C=C), hydroxyl (C-OH), epoxide (C-O-C), carbonyl (C=O), and carboxyl (O=C-O) groups were acted as expected. Before thermal annealing (at room temperature), 45 % of the C=C and 40 % of the C-O-C species existed. As  $T_a$  increased, the amount of C=C species slightly increased but that of C-O-C decreased. An abrupt change was observed at  $T_a = 185$  °C, where the amount of C=C species increased significantly by up to 62 %, but the C-O-C species decreased to 13 %. This is consistent with the expected results in the TGA profile. When  $T_a > 215$  °C, both species changed monotonically while at  $T_a = 300$  °C, the C=C bond increased to over 66 %.

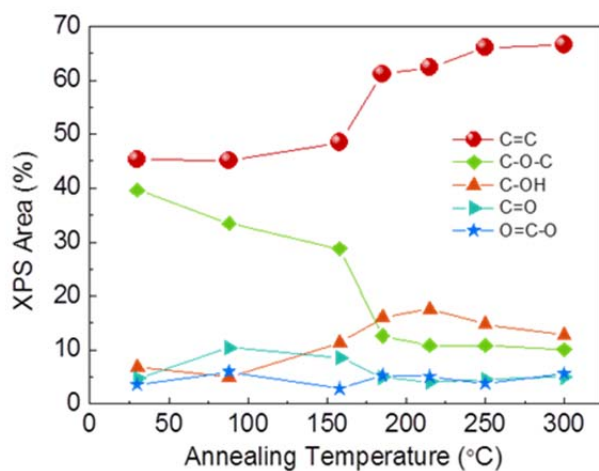


Fig. 3.3. The variation of the amount of carbon and oxygen groups as  $T_a$  increases. The C=C species in MGO was initially 45 % and increased to 66 % after annealing at 300 °C.

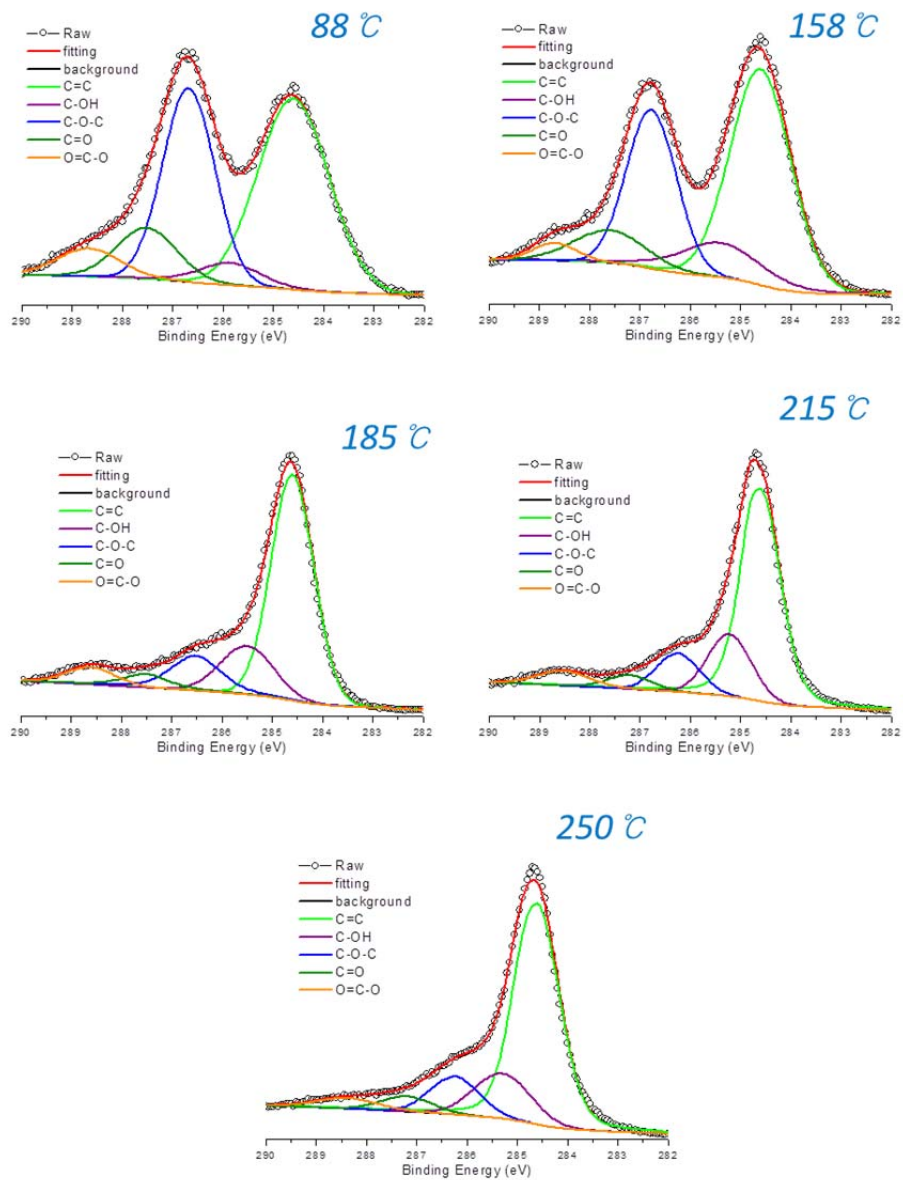


Fig. 3.4. XPS spectra of the MGO at each annealing temperature. At higher  $T_a$ , oxygen functional groups are decreased, and C=C species are restored.

### 3.3.3. Temperature-dependent conductivity of MGO

Temperature-dependent current-voltage ( $I$ - $V$ ) characteristics of MGO were studied and the linear  $I$ - $V$  behaviors were observed at all temperatures. Kaiser *et al.* [22] already mentioned that the resistance of monolayer graphene oxide was not governed by Schottky barrier-limited charge transport (SBCT) which is contact-dominant behavior. Therefore, we checked to make sure that the temperature-dependent conductance ( $G(T)$ ) could not fit the SBCT:

$$G(T) \propto T^{3/2} \cdot e^{(-1/T)} \quad (1)$$

As expected,  $G(T)$  did not follow SBCT, so that we concluded that the obtained  $\sigma$  of the MGO is originated from the intrinsic conduction channel, rather than the contact effect.

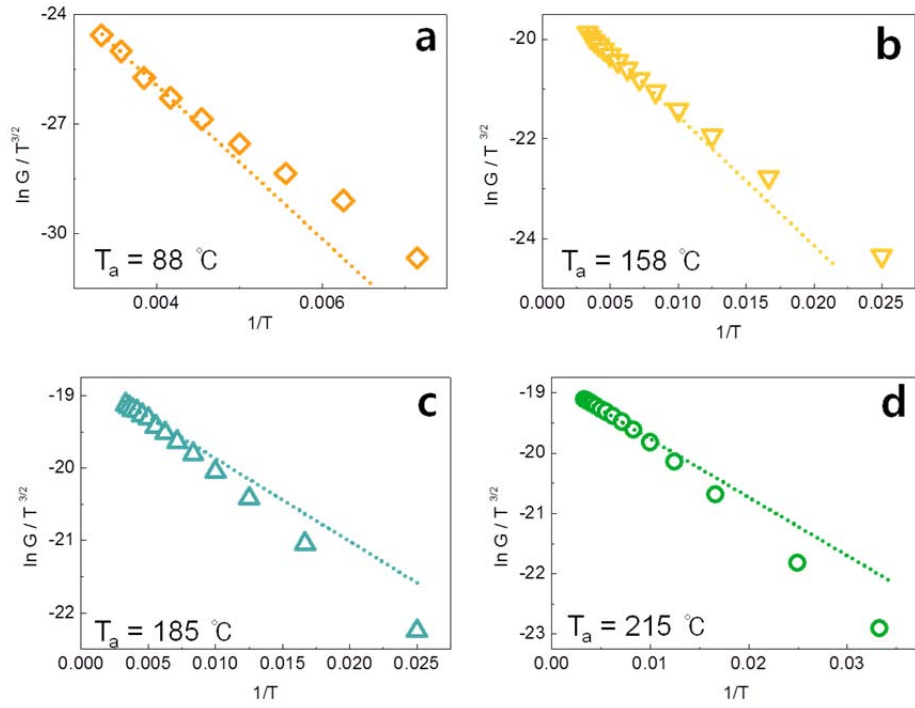


Fig. 3.5. Schottky barrier limited charge transport fitting (plot) of each  $T_a$ . At all  $T_a$ ,  $G(T)$  did not follow SBCT, so that we concluded that the obtained  $\sigma$  of the MGO is originated from the intrinsic conduction channel, rather than the contact effect.

Fig. 3.6(a) represents the normalized  $\sigma(T)$  of the reduced MGO at various  $T_a$  (88, 158, 185, 215, and 250 °C) obtained from the slope in the linear  $I$ - $V$  region. At 300 K, the  $\sigma$  increased about four orders of magnitude upon annealing from 88 °C ( $\sigma = 3.9 \times 10^{-4}$  S/cm) to 250 °C ( $\sigma = 8.90$  S/cm). For the MGO that annealed at 88 °C, the  $\sigma$  abruptly increased with the temperature increase at  $T = 240$  K. In contrast, as  $T_a$  increased, the  $\sigma(T)$  became linear. In each case, the  $\sigma(T)$  extrapolates to zero in the zero-temperature limit, so there are no continuous metal-like conduction paths as is observed in a crystalline monolayer graphene. This shows that the disorder due to oxygen functional groups is sufficient to localize the electronic wave functions across the sample width in parts of the conduction path. The shape change of normalized  $\sigma(T)$  from concave to near linear behavior resembles the behavior observed in disordered conducting polymers and thin carbon nanotube networks [40], but a transition to metallic behavior with non-zero  $\sigma(T)$  in the zero-temperature limit was often observed in those specific cases.

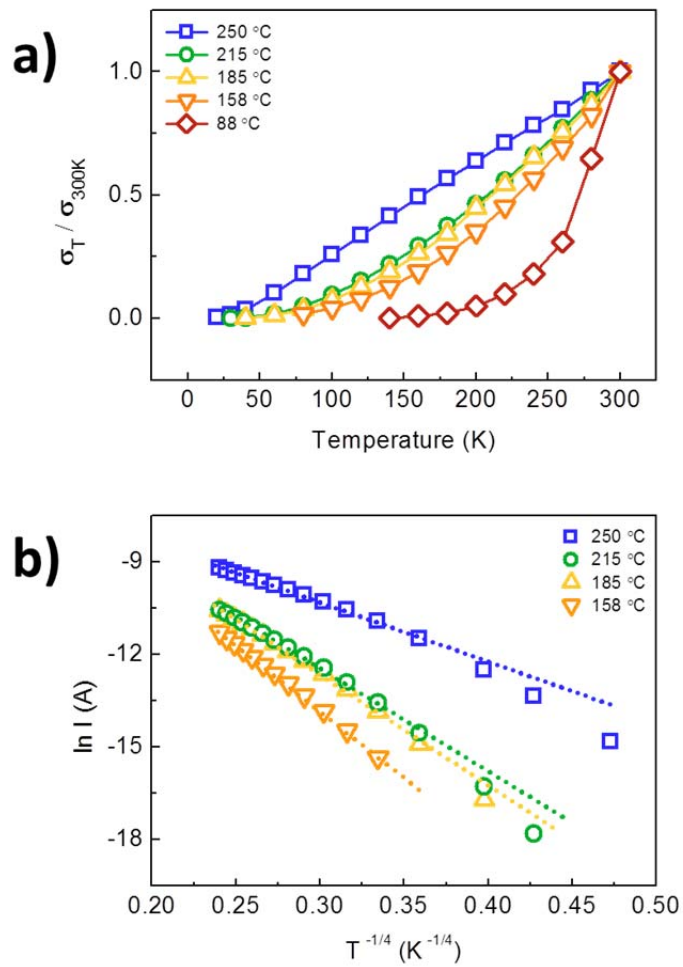


Fig. 3.6. (a) Temperature dependence of normalized  $\sigma$  as a function of  $T_a$ . As  $T_a$  increases, the shape changes from concave to linear. (b) Three dimensional VRH fitting. The three dimensional feature may be caused by the multi-layer of GO. The dotted lines represent extrapolations of the VRH terms in the fits that explain the data at high  $T$ .

The geometric structure of the fully oxidized GO is not yet clearly understood. It was theoretically proposed that the oxygen functional groups on the graphene layer form clusters as mentioned above [40, 41] and was confirmed experimentally [40]. The X-ray photoelectron spectroscopy (XPS) confirmed that the oxygen functional groups decreased as  $T_a$  increased, which causes the decrease in resistivity. The temperature-dependent resistivity of MGO at higher temperatures fits the three dimensional (3D) VRH model (the fit is better suited for 3D expression compared to the two dimensional behavior for GO monolayers [26-29], because the sample used in this report is multilayered GO). Using the clustered oxygen model, we can infer that the GO consists of good conducting regions of graphene domains separated by disordered regions induced by the oxygen functional groups where  $\sigma$  is limited by variable-range hopping.

However, as the temperature lowered, there was a deviation from the VRH behavior at all annealing temperatures. The upward curve of resistivity above the VRH straight line in Fig. 3.7 clearly shows that as the temperature decreases,  $1/T^{1/4}$  increases. This additional resistivity suggests the presence of another resistivity term that increases *faster* than the VRH term when the temperature decreases. Thus, instead of changing to metallic behavior, our MGO flake is showing activated-type conduction. Fig. 3.7 (solid lines) shows this behavior with the presence of an activated resistivity contribution added

in series with the VRH term:

$$\rho_{tot} = \rho_0 \cdot e^{(T_0/T)^{1/4}} + \rho_1 \cdot e^{T_1/T} \quad (2)$$

where  $k_B T_1$  is the activation energy and  $T_0$  is the characteristic temperature inversely proportional to a density of states (DOS).

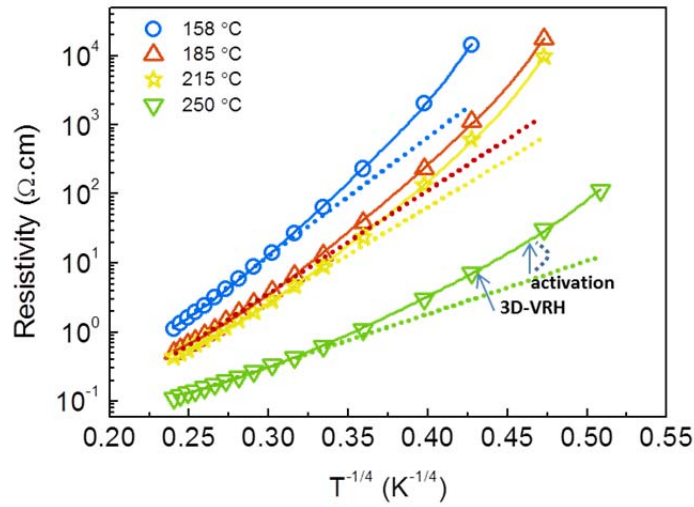


Fig. 3.7. Three dimensional VRH with an added resistivity fitting. Full lines are fit to Eq. (2), and the dotted lines represent extrapolations of the VRH terms in the fits that explain the data at high  $T$ . To see the deviation more clearly, the conductivity is converted to resistivity.

The activated resistivity increases stronger than the VRH term as the temperature decreases, so its effect is only evident at low temperatures. At higher temperatures  $T$  where  $k_B T$  is comparable to or larger than the barrier energy  $k_B T_1$ , the charge carriers easily pass over the barrier. This means the VRH resistivity dominates the sum of resistivity in series. The VRH and activated resistivity terms must be in series to account for the charge transport behavior of the MGO, in contrast to the parallel VRH and activated conduction processes that were observed in some carbon nanotube networks [41]. The fitting parameters for each curve are listed in Table I. It shows that the  $T_0$  and  $T_1$  are gradually reduced as  $T_a$  increases. The decrease of  $T_0$  is clearly understood by the increase of DOS due to the decrease of oxygen functional groups. The activated conduction can be interpreted as follows. Generally, a potential barrier exists at the junction of two materials. In case of GO, a similar potential barrier whose height is proportional to the amount of oxygen functional groups would occur at the domain boundary the clustered oxygen model. In this light, if the desorption of the oxygen functional groups occurs, the potential barrier will decrease and leads to the decrease of  $T_1$ . Hence, we state that the activation energy  $T_1$  is related to the domain boundaries as depicted in Fig. 3.8.

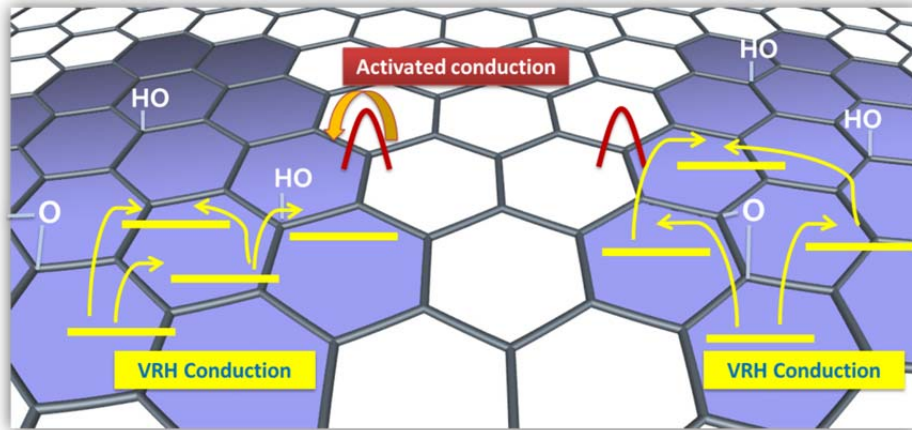


Fig. 3.8. Schematic illustration of the combination model of VRH and activated conduction in series to demonstrate the overall conduction behavior. In shaded area, VRH conduction can occur due to clustered oxygen functional groups. Red clamp is overcoming barrier to conduct between the clustered region.

Table 1. Summary of the fitting parameters for our series VRH and activated model Eq. (2) for conduction in MGO for different annealing temperatures  $T_a$ .

$T_a$ (°C)	$T_0$ (K)	$T_1$ (K)
158	148,757	325
185	101,821	226
215	84,852	217
250	20,057	107

### ***3.3.4. Temperature-dependent conductivity of FGO***

To confirm that this behavior is common in the three dimensional GO but not in monolayer GO, we measured the  $\sigma(T)$  of a few-layer GO (FGO) (Fig. 3.9), where the AFM measurement reveals that it is a trilayer GO (Fig. 3.9(a)). Since the FGO has a small number of layers, we measured the gate voltage-dependent conductivity (Fig. 3.9(b)). As expected, ambipolarity was observed. As  $T_a$  increased, a charge neutrality point was shifted from 30 V for  $T_a = 185$  °C to 20 V for  $T_a = 250$  °C. An increase in mobility was observed, which resulted from the removal of oxygen functional groups by thermal annealing. The hole and the electron mobilities are shown in Fig. 3.10(a). The mobility of the GO annealed at  $T_a = 250$  °C are  $0.93 \text{ cm}^2/\text{V}\cdot\text{s}$  and  $0.65 \text{ cm}^2/\text{V}\cdot\text{s}$  for holes and electrons, respectively. Next, the temperature-dependent resistivity of FGO was measured. We found that the FGO is also well fitted for the combination of the VRH and activation model (Fig. 3.10(b)).

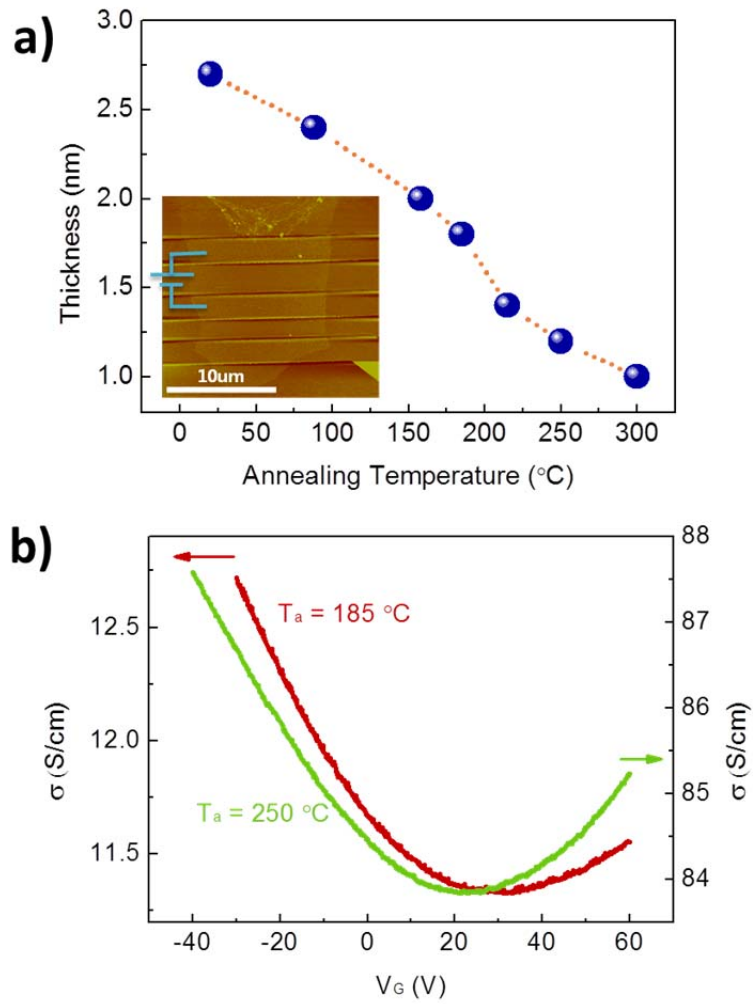


Fig. 3.9. (a) Thickness variation of FGO as a function of  $T_a$  obtained from the AFM study. Inset shows the AFM image of the FGO device. The thickness changes from 2.7 nm to 1.0 nm upon annealing from room temperature to 300 °C (b) Gate voltage-dependent  $\sigma$  of the sample annealed at two different  $T_a$  at 185 (red) and 250 °C (green), as measured at 300 K. Since the sample is FGO, gate dependence is shown clearly and the charge neutrality point was shifted toward 0 V at higher  $T_a$ .

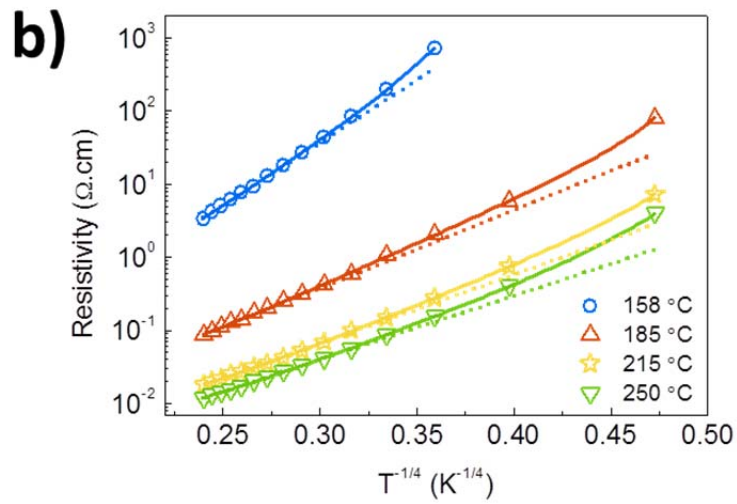
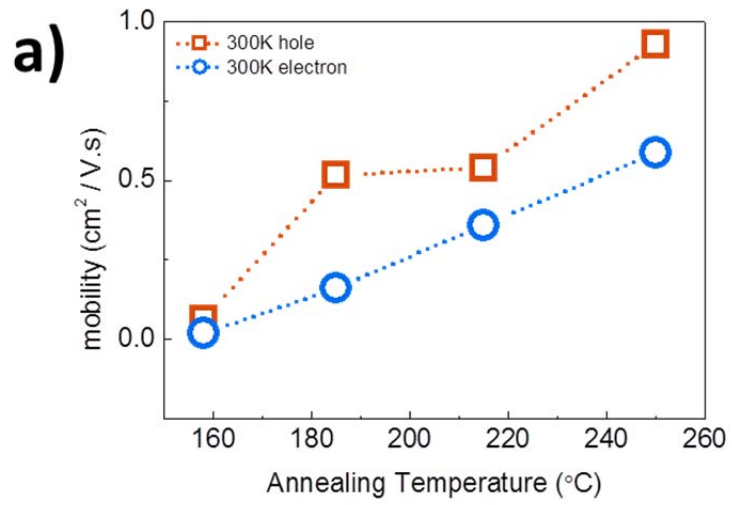


Fig. 3.10. (a) Electron and hole mobilities are shown by taking the slope in  $\sigma - V_G$  curve. In the annealing process, both mobilities increased. (b) Three dimensional VRH with an added resistivity fitting. The dotted lines represent extrapolations of the VRH terms in the fits that explain the data at high  $T$ .

### 3.4. Conclusion

In summary, we have measured the  $\sigma(T)$  of the thermally reduced MGO and FGO as a function of  $T_a$  ( $T_a = 88, 158, 185, 215, 250, \text{ and } 300 \text{ }^\circ\text{C}$ ). The XPS results showed the decomposition of the oxygen functional groups in GO during the annealing procedure. As a result, the  $\sigma(T)$  increases with an increase of  $T_a$ . Unlike in a monolayer GO, the VRH model is not enough to describe the electrical transport of the reduced MGO. A VRH model in series with activation over small energy barriers is appropriate to explain the electrical transport of a reduced MGO. Since the increase of MGO graphitic domain area with an increase of  $T_a$  indicates an increase of the localization length in the VRH, the resistivity decreases at high temperatures. At low temperatures, an additional activated resistivity is observed (in series with the VRH resistivity) and ascribed to the domain boundary in samples.

# Bibliography

- [1] C. R. Dean, A. F. Young, I. Meric, C. Lee, L. Wang, S. Sorgenfrei, K. Watanabe, T. Taniguchi, P. Kim, K. L. Shepard, and J. Hone, *Nat. Nanotechnol.* **5**, 722 (2010).
- [2] C. Lee, X. Wei, J. W. Kysar, and J. Hone, *Science* **321**, 385 (2008).
- [3] A. A. Balandin, *Nat. Mater.* **10**, 569 (2011).
- [4] Z. Z. Zhang, and K. Chang, *Phys. Rev. B* **77**, 235411 (2008).
- [5] C. X. Guo, H. B. Yang, Z. M. Sheng, Z. S. Lu, Q. L. Song, and C. M. Li, *Angew. Chem. Int. Ed.* **49**, 3014 (2010).
- [6] X. Li, X. Wang, L. Zhang, S. Lee, and H. Dai, *Science* **319**, 1229 (2008).
- [7] H. Shi, A. S. Barnard and I. K. Snook, *Phys. Chem. Chem. Phys.* **15**, 4897 (2013).
- [8] J. H. Chen, C. Jang, S. Adam, M. S. Fuhrer, E. D. Williams, and M. Ishigami, *Nature Phys.* **4**, 377 (2008).
- [9] L. Zhao, R. He, K. T. Rim, T. Schiros, K. S. Kim, H. Zhou, C. Gutiérrez, S. P. Chockalingam, C. J. Arguello, L. Pálová, D. Nordlund, M. S. Hybertsen, D. R. Reichman, T. F. Heinz, P. Kim, A. Pinczuk, G. W. Flynn, and A. N. Pasupathy, *Science* **333**, 999 (2011).
- [10] B. H. Kim, S. J. Hong, S. J. Baek, H. Y. Jeong, N. Park, M. Lee, S. W. Lee, M. Park, S. W. Chu, H. S. Shin, J. Lim, J. C. Lee, Y. Jun, and Y. W. Park, *Sci. Rep.* **2**, 690 (2012).

- [11] M. Weser, E. N. Voloshina, K. Horn, and Y. S. Dedkov, *Phys. Chem. Chem. Phys.* **13**, 7534 (2011).
- [12] D. R. Dreyer, S. Park, C. W. Bielawski, and R. S. Ruoff, *Chem. Soc. Rev.* **39**, 228 (2010).
- [13] A. Buchsteiner, A. Lerf, and J. Pieper, *J. Phys. Chem. B* **110**, 22328 (2006).
- [14] D. A. Dikin, S. Stankovich, E. J. Zimney, R. D. Piner, G. H. B. Dommett, G. Evmenenko, S. T. Nguyen, and R. S. Ruoff, *Nature* **448**, 457 (2007).
- [15] H. Chen, M. B. Müller, K. J. Gilmore, G. G. Wallace, and D. Li, *Adv. Mater.* **20**, 3557 (2008).
- [16] J. S. Bunch, A. M. van der Zande, S. S. Verbridge, I. W. Frank, D. M. Tanenbaum, J. M. Parpia, H. G. Craighead, and P. L. McEuen, *Science* **315**, 490 (2007).
- [17] L. Wang, K. Lee, Y. Sun, M. Lucking, Z. Chen, J. J. Zhao, and S. B. Zhang, *ACS Nano* **3**, 2995 (2009).
- [18] J. W. Burress, S. Gadipelli, J. Ford, J. M. Simmons, W. Zhou, and T. Yildirim, *Angew. Chem. Int. Edit.* **49**, 8902 (2010).
- [19] B. H. Kim, W. G. Hong, H. Y. Yu, Y. Han, S. M. Lee, S. J. Chang, H. R. Moon, Y. Jun, and H. J. Kim, *Phys. Chem. Chem. Phys.* **14**, 1480 (2012).
- [20] S. Chen, J. Zhu, X. Wu, Q. Han, and X. Wang, *ACS Nano* **4**, 2822 (2010).
- [21] J. T. Robinson, F. K. Perkins, E. S. Snow, Z. Wei, and P. E. Sheehan, *Nano Lett.* **8**, 3137 (2008).

- [22] D. Luo, G. Zhang, J. Liu, and X. Sun, *J. Phys. Chem. C* **115**, 11327 (2011).
- [23] S. Saxena, T. A. Tyson, and E. Negusse, *J. Phys. Chem. Lett.* **1**, 3433 (2010).
- [24] C. Gómez-Navarro, J. C. Meyer, R. S. Sundaram, A. Chuvilin, S. Kurasch, M. Burghard, K. Kern, and U. Kaiser, *Nano Lett.* **10**, 1144 (2010).
- [25] K. A. Mkhoyan, A. W. Contryman, J. Silcox, D. A. Stewart, G. Eda, C. Mattevi, S. Miller, and M. Chhowalla, *Nano Lett.* **9**, 1058 (2009).
- [26] G. Eda, C. Mattevi, H. Yamaguchi, H. Kim, and M. Chhowalla, *J. Phys. Chem. C* **113**, 15768 (2009).
- [27] G. Venugopal, K. Krishamoorthy, R. Mohan, and S. Kim, *Mater. Chem. Phys.* **132**, 29 (2010).
- [28] C. Gómez-Navarro, R. T. Weitz, A. M. Bittner, M. Scolari, A. Mews, M. Burghard, and K. Kern, *Nano Lett.* **7**, 3499 (2007).
- [29] A. B. Kaiser, C. Gómez-Navarro, R. S. Sundaram, M. Burghard, and K. Kern, *Nano Lett.* **9**, 1787 (2009).
- [30] D. Joung, and S. I. Khondaker, *Phys. Rev. B* **86**, 235423 (2012).
- [31] T. Q. Trung, N. T. Tien, D. Kim, J. H. Jung, O. J. Yoon, and N. Lee, *Adv. Mater.* **24**, 5254 (2012).
- [32] S. Wang, H. E. Lin, H. Lin, K. Y. Chen, K. Tu, C. W. Chen, J. Chen, C. Liu, C. Liang, and Y. F. Chen, *Nanotechnology* **22**, 335701 (2011).
- [33] B. Fugetsu, E. Sano, H. Yu, K. Mori, and T. Tanaka, *Carbon* **48**, 3340 (2010).

- [34] J. Yan, and M. Y. Chou, *Phys. Rev. B* **82**, 125403 (2010).
- [35] M. Topsakal, and S. Ciraci, *Phys. Rev. B* **86**, 205402 (2012).
- [36] S. S. Han, H. Jung, D. H. Jung, S. Choi, and N. Park, *Phys. Rev. B* **85**, 155408 (2012).
- [37] S. Hummers, and R. E. Offeman, *J. Am. Chem. Soc.* **80**, 1339 (1958).
- [38] H. Jeong, Y. P. Lee, R. J. W. E. Lahaye, M. Park, K. An, I. J. Kim, C. Yang, C. Y. Park, R. S. Ruoff, and Y. H. Lee, *J. Am. Chem. Soc.* **130**, 1362 (2008).
- [39] A. B. Kaiser and V. Skákalová, *Chem. Soc. Rev.* **40**, 3786 (2011).
- [40] K. Erickson, R. Erni, Z. Lee, N. Alem, W. Gannett, and A. Zettl, *Adv. Mater.* **22**, 4467 (2010).
- [41] S. Ravi, A. B. Kaiser and C. W. Bumby, *Physica Status Solidi B* **250**, 1463 (2013).

# **Chapter 4**

## **Electrical Conduction of Palladium-decorated Multi-layered Graphene Oxide Effected by Hydrogen Dissociation**

### **4.1. Introduction**

Energy and environmental problems regarding fossil fuel depletion, pollution, and global warming are currently hot topics. The development of variable electronic devices requires smaller and highly efficient energy storage capabilities. For this reason, energy related storage methods like super-capacitors, secondary batteries, and hydrogen fuel cells have increasingly attracted attention. In particular, hydrogen fuel cell technology has emerged as a strong candidate to replace and supplement batteries in portable applications by offering numerous benefits over the most advanced existing batteries. Fuel cells produce electricity through a reaction between fuels (cathode) continuously supplied from an external source and an oxidant

(anode). Traditionally, fuel cells consist of hydrogen/oxygen cells and methanol/oxygen cells. The most common material as catalyst in fuel cells is Pt and the electricity is generated by hydrogen and methanol oxidation. The fuel cells can be operated at low temperature. A problem is that Pt is expensive, leading to limitations in commercialization. Due to the high surface area and excellent dispersibility for maintaining stable catalysts, carbon based materials such as carbon black [1], carbon nanotubes [2, 3] and graphene [4] have been extensively studied for use as energy related materials. For example, the graphene / Pt complex is based on oxygen reduction and methanol oxidation cells. They are catalytically more efficient than the carbon black (Vulcan XC-72) used in commercial markets [5, 6]. Recently, the graphene nanoribbon / carbon fiber / Pt complex [7] and nitrogen-doped graphene / Pt complex [8] have been introduced. Graphene has excellent electrical and structural characteristics for a two-dimensional nanostructure. This enables electron and ion transport through the graphene surface. Pt particle sizes can be controlled to 0.5 nm or less by using graphene. Because Pt nanoparticles are bonded to the graphene surface without agglomeration [9], it is possible to minimize the amount of Pt. This improves fuel cell efficiency due to an increase in the Pt nanoparticle surface area when used as the catalyst. Since Pt is expensive, however, several studies have looked for a Pt replacement. By a simple preparation method using carbon nanosheets with

Pd [10], Ag [11], Pd-Au [12], Pd-Ni [13] and Pt-Pd [14] particles, better results than those achieved by Pt could be obtained. In particular, Pd has been evaluated as an alternative to Pt due to its very good electrochemical performance in methanol and ethanol oxidation and lower cost [15, 16].

Meanwhile, graphene oxide (GO) is used significantly in graphene production. GO is also an important material with various potential applications. In earlier days, many studies focused on obtaining large quantities of high quality material near graphene through GO reduction. However, many recent studies show interesting functions by the GO itself. Oxygen functional groups and defects in GO can modulate its properties by a chemical reaction with oxygen groups or interacting with defects. In addition, the high reactivity of oxygen functional groups allows an ability to oxidize other substances. It can also increase interaction of metal nanoparticles adsorbed onto the GO surface and produces new functional groups [17]. Other studies addressed well-dispersed Pd particles to improve the catalytic efficiency of fuel cells [18-20], making Pd-embedded three dimensional GO structures [21] and hydrogen sensors [22, 23]. Previous studies, however, rarely report on the variation in electrical conductivity of Pd-decorated MGO (PdGO), the fundamental property of PdGO, under hydrogen environment.

The pressure-dependent electrical conductance (G) of MGO and PdGO during H<sub>2</sub> exposure (up to 20 bar) is examined along with the release

process. As the H<sub>2</sub> pressure increases, the G of MGO increases while G of PdGO decreases. The MGO and PdGO before and after hydrogen exposure are examined by AFM, XPS, and FT-IR. The increase in G of MGO may be explained similarly as an annealing of graphene in hydrogen atmosphere. The decrease of G in PdGO may come from a decrease of the C/O ratio (carbon to oxygen ratio) by OH groups, which oxidize the PdGO surface and are formed when PdO is reduced by hydrogen

## **4.2. Experimental**

### ***4.2.1. MGO and PdGO sheets fabrication***

MGO sheets were prepared by utilizing the Hummers method [24] and PdGO sheets synthesized by Suzuki-Miyaura coupling reaction with mixing of the MGO sheets and Pd acetate (1.1 mmol) in water [25]. The generation of Pd nanoparticles within the MGO support was done by bubbling hydrogen through a suspension of Pd<sup>2+</sup>-MGO in ethanol. After evaporation of solvent, we obtained powder type PdGO. Again, PdGO was dispersed in water and then hydrazine hydrate (N<sub>2</sub>H<sub>5</sub>OH, 99.9 %) was added to a suspension of PdGO. After being stirred overnight, the solution was centrifuged and washed several times. The residue was dried in vacuum at 40 °C. Then, the byproduct was heated up to 600 °C under Ar atmosphere. The detailed synthesizing procedure is described in *ref.* 25.

The MGO (PdGO) devices were fabricated by drop casting, which is applicable for a wide range of substrates. The MGO (PdGO) sheets were obtained via ultra-sonication in deionized water using a sonicator before the solution was centrifuged at 10,000 rpm for 5 minutes. Then, the supernatant was dropped onto a highly p-doped ( $\rho < 0.005 \Omega \cdot \text{cm}$ ) silicon wafer covered by a thermally grown  $\text{SiO}_2$  layer (300 nm thickness). Before it was fully dried, the solution was blown off with  $\text{N}_2$  gas to avoid a densely packed MGO layer. A conventional electron-beam lithography (VEGA MM5150 with 30 keV, TESCAN) and Ti/Au (5/50 nm) was deposited on top of the MGO (PdGO) using the thermal evaporation system (MHS-1800, Muhan Vacuum) in order to define the electrode.

#### ***4.2.2. Device preparation***

The MGO needs to be reduced as it is nearly insulating. The devices were placed on a horizontal tube-type furnace (Ajeon Heating Industry) to reduce the MGO in a flow of Ar. Before thermal annealing was conducted, we pumped out the chamber ( $< 10^{-2}$  Torr) to remove any remaining gas or water in the air. The flow rate of Ar gas was 100 sccm and thermal annealing was performed at 250 °C for 2 hours. In prior to measurement, the samples were evacuated ( $< 10^{-6}$  Torr) with heating (100 °C) for 4 hrs. A tapping mode AFM at 0.3 Hz confirmed the increase in the MGO sheet's height after the hydrogen

exposure. XPS (Sigma Probe, VG Scientific) was also carried out to compare the components of carbon bonds in the MGO sheet before and after hydrogen exposure.

#### ***4.2.3 Electrical measurement***

The H<sub>2</sub> pressure-dependent conductance was measured with a semiconductor characterization system (SCS-4200, Keithley) at 300 K. The H<sub>2</sub> pressure was increased up to 20 bar (2 bar steps per hour). After one hour at 20 bar, the H<sub>2</sub> pressure was released at the same rate and pumped out. At 300 K, the resistance of the MGO and PdGO devices is in the MΩ range. Therefore, we measured the devices by a two-probe method. In our previous study on electrical properties of the MGO, we showed that  $G$  was governed by intrinsic channel, rather than contact effect [26]. We focused on the change of the  $G$  of the MGO and PdGO devices. There is an about twenty times difference of  $G$  between MGO and PdGO devices, but it can vary between different samples. Even though the MGO (and PdGO) sheets were made in the same one-pot process, the  $G$  of the devices is varied by one order.

## 4.3. Results and Discussion

### 4.3.1. *Electrical conductance of pristine MGO at high pressure H<sub>2</sub> gas*

First, to apprehend the conductivity characteristics of the interaction between H<sub>2</sub> and PdGO, we measured H<sub>2</sub> pressure-dependent  $G$  of MGO. The H<sub>2</sub> pressure varies from vacuum to 20 bar using a high pressure chamber at 300 K. Fig. 4.1(a) shows an AFM image of the MGO, which has 7 layers (8.76 Å / layer from XRD). To show the sample configuration clearly, we draw the yellow dashed line as guideline. Upon exposure to H<sub>2</sub>, the average thickness changes from 6.9 nm to 6.5 nm (about 6 % decreased). The H<sub>2</sub> exposure can cause desorption of oxygen functional groups and a decrease in interlayer spacing. Fig. 4.1(b) shows H<sub>2</sub> pressure-dependent  $G$  of MGO. Even after high vacuum ( $\sim 10^{-6}$  Torr, pressure = 0 indicates high vacuum in figures), the  $G$  did not return to the original value obtained before H<sub>2</sub> exposure. The increase in  $G$  can be explained by the same MGO reduction in H<sub>2</sub> atmosphere since H<sub>2</sub> is known as an effective annealing agent in GO thermal reduction [27].

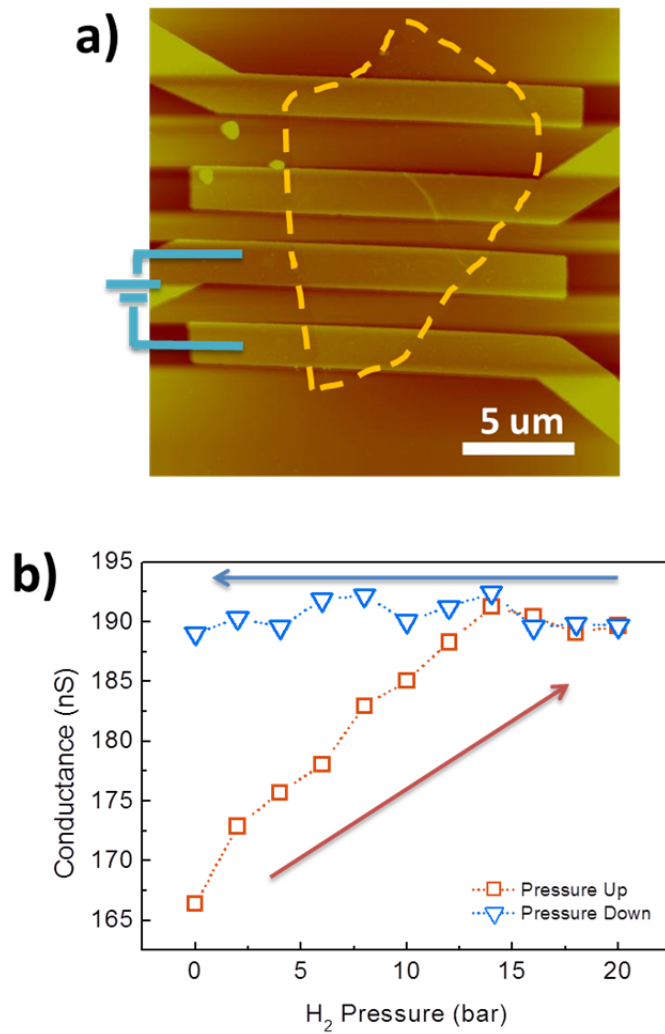


Fig. 4.1. (a) The AFM image of the MGO. The AFM reveals it has 7 layers with an average thickness from 6.9 nm to 6.5 nm after H<sub>2</sub> exposure. (b) The  $G$  of MGO during hydrogen exposure and release. The  $G$  increases as hydrogen pressure increases, while it remains with little change during the release process. The  $G$  does not recover even at high vacuum.

### ***4.3.2. XPS spectra of pristine MGO***

To support this suggestion, XPS was carried out. The XPS analysis can provide direct evidence of the chemical environment of excited atoms. Fig. 4.2(a), and (b) shows C 1s spectra of MGO before and after H<sub>2</sub> exposure. In the C 1s XPS spectra of MGO, there are five different types of carbon and oxygen related bonds of C=C (284.6 eV), C-OH (285.6 eV), C-O-C (286.7 eV), C=O (288.0 eV), and O=C-O (288.9 eV) in MGO [28, 29]. Unfortunately, the shape of two peaks – the C 1s peaks before and after H<sub>2</sub> exposure – are more or less the same. This means that it is not easy to analyze the chemical composition of MGO. From the area integration values, we found that the amount of C=C bonds increases while oxygen functional groups decrease after H<sub>2</sub> exposure (Fig. 4.2(d)). A high pressure H<sub>2</sub> environment acts as an annealing agent to reduce the MGO. G increases 15 % even though very small amounts of hydrogen functional groups are varied. Therefore, hydrogen would significantly affect the *G* of MGO.

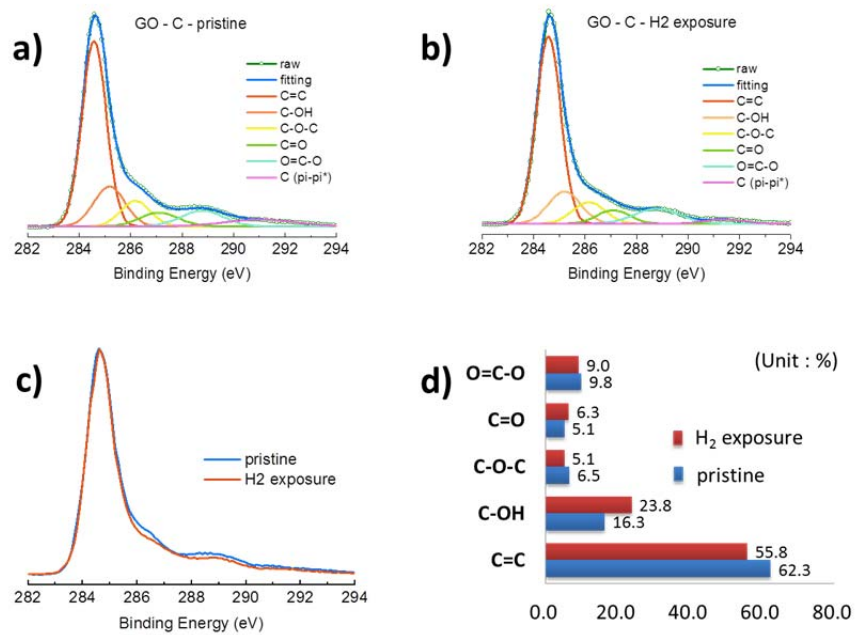


Fig.4.2. C 1s XPS spectra of MGO before (a) and after (b) hydrogen exposure. Analyzed peaks indicate different types of carbon species, C=C (284.6 eV), C-OH (285.6 eV), C-O-C (286.7 eV), C=O (288.0 eV) and O=C-O (288.9 eV) in pristine MGO. (c) To compare the C 1s spectra of before and after H<sub>2</sub> exposure, the peaks are plotted simultaneously ((a) and (b)). (d) The amount of carbon species are evaluated from area weights in XPS spectra.

### ***4.3.3. Electrical conductance of PdGO at high pressure H<sub>2</sub> gas***

The high-resolution TEM image shows Pd nanoparticles with 2-3 nm diameters that are attached to the MGO surface (Fig. 4.3(a)). The lattice fringes can be seen in the nanoparticles, as shown in the magnified Fig. 4.3(a). The fringe spacing, interplanar spacing of 0.23 nm, corresponds to the {111} spacing planes of Pd. To investigate the interaction between H<sub>2</sub> and PdGO, we followed the same measurement procedure used in MGO. Contrary to the situation for MGO, we found a decrease of  $G$  of PdGO as the H<sub>2</sub> pressure increases and  $G$  did not recover as the pressure was released, even in vacuum condition. This behavior is similar to the pressure-dependent current variation in Pd-doped vanadium oxide nanowires (Pd-VONs) reported in 2010 [30]. In Pd-VONs, an electric current suppression occurred during H<sub>2</sub> exposure. It comes from the electron transfer from VON to PdO when PdO is reduced by dissociated hydrogen atoms. To elucidate the dissociation effect, the states of PdGO before and after hydrogen exposure were investigated by AFM, XPS, and FT-IR spectroscopy. From the AFM analysis, PdGO is revealed to have 13 layers and the average thickness is increased from 11.0 nm to 13.7 nm (24 % increased) after H<sub>2</sub> exposure. The remarkable point is that PdGO increases in thickness during H<sub>2</sub> exposure.

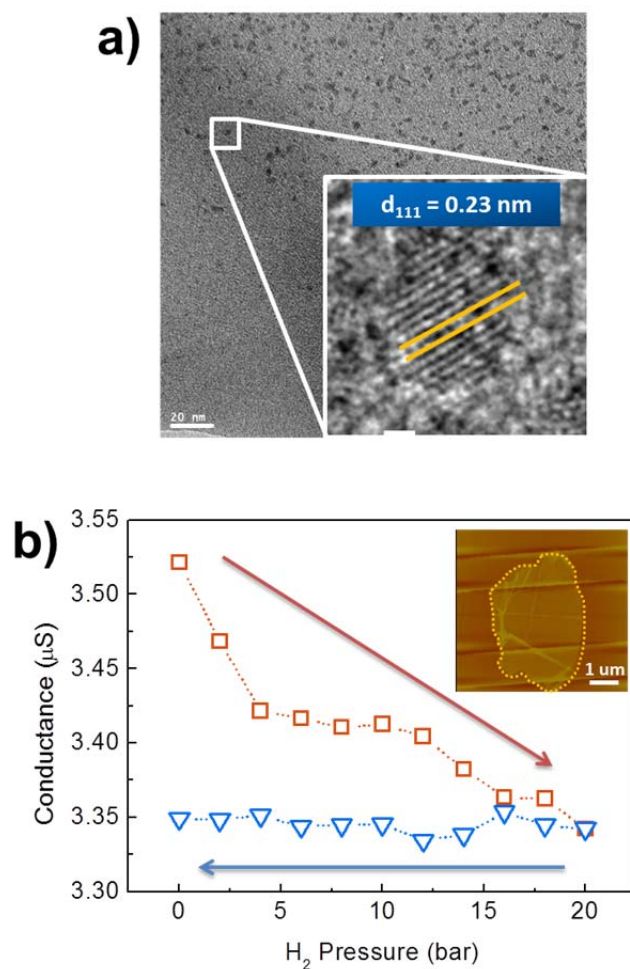


Fig. 4.3. (a) A transmission electron microscopy image shows that the MGO surface is decorated by Pd nanoparticles. The magnified image shows that the crystallized nanoparticles (2-3 nm) are Pd particles whose interplanar spacing is 0.23 nm (between yellow lines). Scale bar: 20 nm (b) The  $G$  of PdGO during hydrogen exposure and release. The  $G$  decreases as  $H_2$  pressure increases but remains the same, with little change, as the pressure is released. Pressure-dependent  $G$  of the PdGO tends to go in the opposite direction (compared to the MGO). The AFM image of the inset reveals that PdMGO has 13 layers and the average thickness changes from 11.0 nm to 13.7 nm (24 % increased) after  $H_2$  exposure.

#### 4.3.4. XPS spectra of Pd 3d of PdGO

The XPS peak position and area tell us the elemental identification and chemical state of element, and relative composition of the constituents. Fig. 4.4(a) and (b) show the XPS spectra of Pd before and after hydrogen exposure ( $3d_{5/2}$  (335.5  $\rightarrow$  335.3 eV),  $3d_{3/2}$  (340.5  $\rightarrow$  340.7 eV)). PdO ( $\text{Pd}^{2+}$   $3d_{5/2}$ : 337.3 eV), PdO<sub>2</sub> ( $\text{Pd}^{4+}$   $3d_{5/2}$ : 338.4 eV) peaks may come from Pd oxidation as soon as Pd nanoparticles are exposed to air. When H<sub>2</sub> is adsorbed on the surface, the binding energy of Pd and PdO are decreased by 0.2 eV (Pd  $3d_{5/2}$  : 335.5  $\rightarrow$  335.3 eV, PdO :  $\text{Pd}^{2+}$   $3d_{5/2}$ : 337.3  $\rightarrow$  337.1 eV). This means that PdO is reduced by H<sub>2</sub> adsorption. Furthermore, the relative area of PdO (+PdO<sub>2</sub>) decreases from 62.9 % to 56.6 %, but Pd increases in area from 37.1 % to 43.4 % after H<sub>2</sub> exposure, which may explain PdO (PdO<sub>2</sub>) reduction. The peaks, particularly the Pd one, are broadened substantially after the sample has been exposed to H<sub>2</sub>. Broadening of a peak indicates a change in the amount of chemical bonds contributing to the peak shape, and a change in the sample condition (X-ray damage) and/or differential charging of the surface. Amounts of C=C bonds are decreased and C-OH bonds increased after H<sub>2</sub> exposure. The additional C bonds in Fig. 4.4(c) and (d) changed relatively less and cannot be distinguished in an analysis. The C-OH peak is broadened more by H<sub>2</sub> than the C=C one. The behavior can be interpreted as a decrease in the C=C bonds of PdGO when C-OH bonds are formed by combining with C

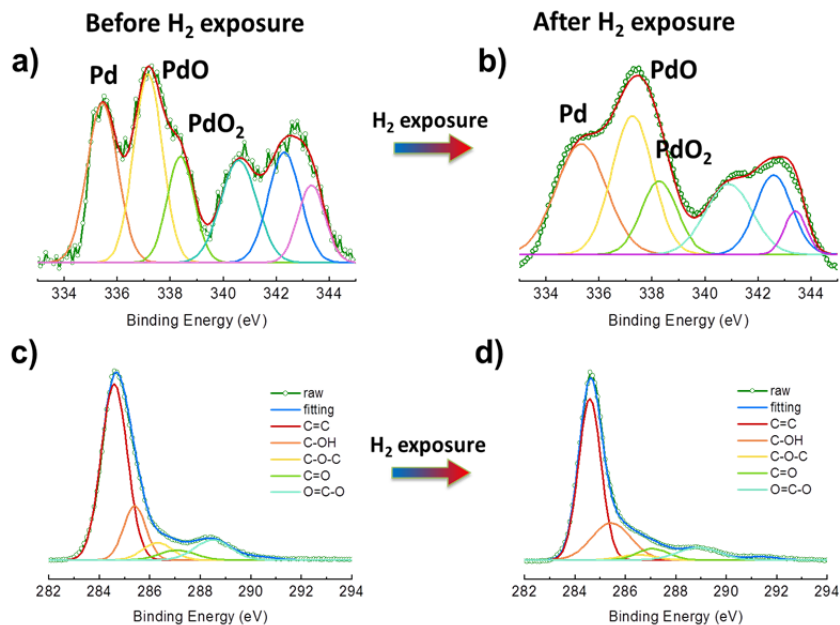
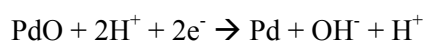


Fig. 4.4. The XPS spectra for Pd 3d of the PdGO (a) before and (b) after H<sub>2</sub> exposure. When the PdGO is exposed to H<sub>2</sub>, the amounts of PdO (337.3 eV) and PdO<sub>2</sub> (338.4 eV) decrease and Pd (335.5 eV) peak increases. The relative weight of Pd increases, indicating PdO reduction. (c) and (d) show XPS spectra of PdGO for C 1s before and after H<sub>2</sub> exposure. The five species bonding, C=C, C-OH, C-O-C, C=O and O=C-O, are shown in C 1s spectra. The amount of C-OH bonding increases but C=C bonding decreases after H<sub>2</sub> exposure to the PdGO. Secondary peaks in (a) and (b) show the same behavior as the primary ones.

atoms and dissociated hydrogen atoms. Similar results can be found in previous works. Recently, the interaction between H<sub>2</sub> and PdO film surface was investigated [31] and OH group formation was observed as soon as the PdO film was exposed to H<sub>2</sub>. The PdO was experimentally observed to be reduced when H<sub>2</sub> was adsorbed onto the PdO at room temperature. In light of the results, PdO (PdO<sub>2</sub>) is expected to be reduced as H<sub>2</sub> pressure increases. The reduction process is described in the following (similar to our previous study on Pd-VONs):



First, the PdO is formed through the partial oxidation of decorated Pd. When H<sub>2</sub> is adsorbed on the PdGO surface, dissociation occurs on (unoxidized) Pd surface and electrons are generated. The PdO (PdO<sub>2</sub>) is reduced to Pd by binding the produced electrons and Pd<sup>2+</sup> (Pd<sup>4+</sup>). The hydrogen atoms form OH groups by binding with PdO oxygen and then re-formed by a C-OH bond. Therefore, the MGO supporting material is oxidized even more by the generated oxygen functional groups induced from hydrogen adsorption. As a result, *G* of PdGO is decreased by decreasing the sole carbon region (C/O ratio decreased). Since the *G* does not recover even at high vacuum (~10<sup>-6</sup> Torr), we expect the reverse process not to occur at room temperature. This is a spillover effect. The hydrogen molecules are chemisorbed on dispersed Pd nanoparticles and dissociated, and then the

dissociated hydrogen atoms migrate to the PdGO and diffuse further. The hydrogen atoms break carbon bonds and produce C-OH bonds

#### **4.3.5. FTIR spectra of PdGO**

FT-IR measurements investigate the bonding interactions in PdGO before and after hydrogen exposure (Fig. 4.5). The PdGO spectra show typical features at  $\sim 1060\text{ cm}^{-1}$  (C-O),  $\sim 1228\text{ cm}^{-1}$  (-OH; in alcohol),  $\sim 1395\text{ cm}^{-1}$  (C-O; in carboxyl),  $\sim 1627\text{ cm}^{-1}$  (C=C), and  $\sim 1720\text{ cm}^{-1}$  (C=O) [32, 33]. After hydrogen adsorption, a new peak appears at  $1220\text{ cm}^{-1}$  due to C-OH bond formation. A broad and weak peak between 2000 and 2500 shows the carbon triple bond transformed from a different carbon bond (from single / double bond to triple bond). A strong and broad peak can be seen, particularly in the non-exposed sample, between  $3000$  and  $3700\text{ cm}^{-1}$  in the high frequency area corresponding to the stretching vibration of water molecule OH groups on the PdGO [34]. The decrease of the broad peak region in *ca.*  $3000 - 3700\text{ cm}^{-1}$  is consistent with C-OH formation.

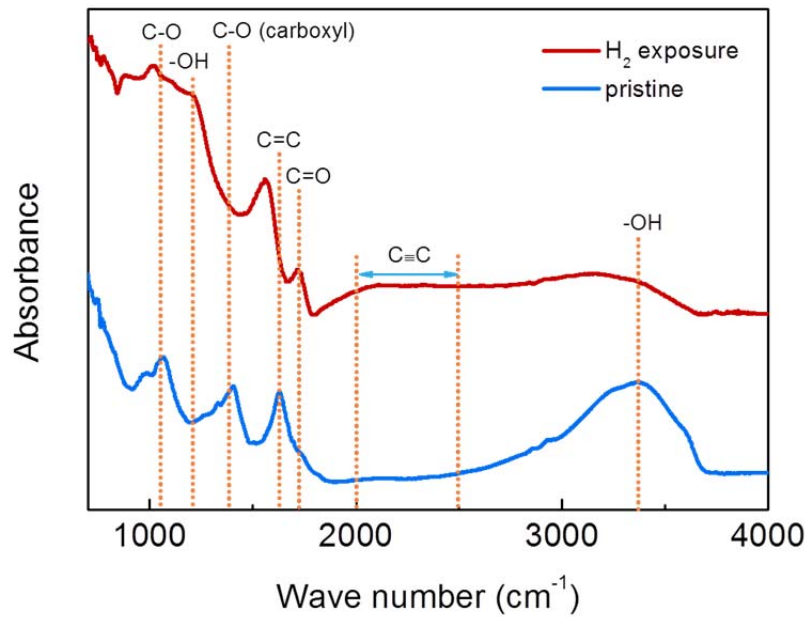


Fig. 4.5. FTIR spectra of PdGO before and after H<sub>2</sub> exposure.

An alternative explanation of the decrease in  $G$  by exposing PdGO to H<sub>2</sub> is following. Before H<sub>2</sub> exposure, the  $G$  of PdGO is considerably higher than MGO. This suggests that the  $G$  in the Pd particles dominate possible problems from electrical contacts to the GO matrix. And the Pd particles on the surface could also improve contacts to the electrodes. Now, upon H<sub>2</sub> exposure, one may expect the  $G$  to increase as the PdO part is reduced to Pd by H<sub>2</sub>. However, hydrogen is known to be readily dissolved in Pd in interstitial positions, which

would lead to resistance to increase. The dissolved hydrogen in Pd cannot be pumped out in high vacuum. Therefore, the  $G$  does not return to its initial value when the hydrogen gas is pumped out. This explanation is supported by the increase in effective thickness of PdGO and the width of the XPS Pd peak upon  $H_2$  exposure. Hydrogen is so light, the peak of PdH is so close to Pd (0.3 eV higher than Pd). Hence, it is not possible to extract PdH from the Pd peak in XPS data fitting. On the other hand, the change in the C-OH bond shown in Fig. 3 (c), (d) is significantly bigger compared with the Pd peak change in Fig. 3(b). We conclude that the above effect of  $H_2$  dissolved Pd is not major mechanism for the  $G$  decrease.

#### 4.4. Conclusion

We have presented an experimental study of the hydrogen pressure-dependent  $G$  in the MGO and PdGO. As the hydrogen gas pressure increases, the  $G$  of MGO also increases while it decreases in PdGO. To elucidate the interaction between high pressure hydrogen molecules and PdGO, the states of MGO and PdGO before and after hydrogen exposure were investigated through AFM, HRTEM, XPS, and FT-IR analysis. In MGO, we explained the oxygen functional group desorption that is similar to the annealing effect. Meanwhile, the hydrogen molecules are chemisorbed on dispersed Pd nanoparticles and dissociated in PdGO and the dissociated hydrogen atoms interact with PdO and form OH groups. The OH groups combine with carbon in PdGO and produce C-OH bonds. As a result, the  $G$  of PdGO decreases due to the decreased C/O ratio and more oxidized states induced by C-OH bonds. The conductivity of the Pd particles themselves may also be affected by a hydrogen uptake. Our study has elucidated the properties of PdGO when exposed to  $H_2$  and improved the understanding of the role by PdGO in applications like gas sensors and fuel cells.

## Bibliography

- [1] G. Faubert , G. Lalande, R. Cote, D. Guay, J. P. Dodelet, L. T. Weng, P. Bertrand, and G. Denes, *Electrochimica Acta* **41**, 1689 (1996)
- [2] Zhaolin Liu, Xuanhao Lin, Jim Yang Lee, Weide Zhang, Ming Han, and Leong Ming Gan, *Langmuir* **18**, 4054 (2002)
- [3] Cheng Wang, Mahesh Waje, Xin Wang, Jason M. Tang, Robert C. Haddon, and Yushan Yan, *Nano Lett.* **4**, 345 (2004)
- [4] Liangti Qu, Yong Liu, Jong-Beom Baek, and Liming Dai, *ACS Nano* **4**, 1321 (2010)
- [5] Brian Seger, and Prashant V. Kamat, *J. Phys. Chem. C* **113**, 7990 (2009)
- [6] Aditi Halder, Sudhanshu Sharma, M. S. Hegde, and N. Ravishankar, *J. Phys. Chem. C* **113**, 1466 (2009)
- [7] Chaonan Wang, Hongrong Gao, Hong Li, Yiren Zhang, Bowen Huang, Junhong Zhao, Yan Zhu, Wang Zhang Yuan, and Yongming Zhang, *Nanoscale* **6**, 1377 (2014)
- [8] Ding Ding, Zhi-Ling Song, Zhen-Qian Cheng, Wei-Na Liu, Xiang-Kun Nie, Xia Bian, Zhuo Chen, and Weihong Tan, *J. Mater. Chem. A* **2**, 472 (2014)
- [9] EunJoo Yoo, Tatsuhiro Okata, Tornoki Akita, Masanori Kohyama, Junji Nakamura, and Itaru Honma, *Nano Lett.* **9**, 2255 (2009)

- [10] Zhong-Liang Hu, Mami Aizawa, Zheng-Ming Wang,\* Noriko Yoshizawa, and Hiroaki Hatori, *Langmuir* **26**, 6681 (2010)
- [11] Chuilin Lai, Praveen Kolla, Yong Zhao, Hao Fonga, Alevtina L. Smirnova, *Electrochimica Acta* **130**, 431 (2014)
- [12] Feihui Li, Yongqin Guo, Ruqiang Li, Fei Wu, Yu Liu, Xiyang Sun, Chuangbao Li, Wei Wang, and Jianping Gao, *J. Mater. Chem A* **1**, 6579 (2013)
- [13] Remegia M. Modibedi, Mkhulu K. Mathe, Rapelang G. Motsoeneng, Lindiwe E. Khotseng, Kenneth I. Ozoemena, Eldah K. Louw, *Electrochimica Acta* **128**, 406 (2014)
- [14] Shan-Shan Li, Jing-Jing Lv, Yuan-Yuan Hu, Jie-Ning Zheng, Jian-Rong Chen, Ai-Jun Wang, Jiu-Ju Feng, *J. Power Sources* **247**, 213 (2014)
- [15] Yuan-Hang Qin, Hou-Hua Yang, Xin-Sheng Zhang, Ping Li, Chun-An Ma, *Inter. J. Hydrogen Energy* **35**, 7667 (2010)
- [16] Changwei Xu, Liqiang Cheng, Peikang Shen, Yingliang Liu, *Electrochem. Commun.* **9**, 997 (2007)
- [17] Gyubong Kim, and Seung-Hoon Jhi, *ACS Nano* **5**, 805 (2011)
- [18] Jingjing Lin, Tao Mei, Meijiao Lv, Chang'an Zhang, Zhenfeng Zhao and Xianbao Wang, *RSC Adv.* **4**, 29563 (2014)
- [19] Sudong Yang, Jing Dong, Zhaohui Yao, Chengmin Shen, Xuezhao Shi, Yuan Tian, Shaoxiong Lin, and Xiaogang Zhang, *Scientific reports* **4**, 1 (2014)
- [20] Shun-ichi Yamamoto, Hiroshi Kinoshita, Hideki Hashimoto, and Yuta Nishina, *Nanoscale* **6**, 6501 (2014)

- [21] Xizheng Wang, Wufeng Chen, and Lifeng Yan, *Mater. Chem. Phys.* **148**, 103 (2014)
- [22] Min Gyun Chung, Dai-HongKim, DongKyun Seo, TaewooKim, Hyeong Uk Im, Hyun Myoung Lee, Ji-Beom Yoo, Seong-Hyeon Hong, Tae June Kang, and Yong Hyup Kim, *Sensors and Actuators B* **169**, 387 (2012)
- [23] P.A. Pandey, N.R.Wilson, J.A. Covington, *Sensors and Actuators B* **183**, 478 (2013)
- [24] Williams. Hummers, and Richard E. Offeman, *J. Am. Chem. Soc.* **80**, 1339 (1958).
- [25] Gil M. Scheuermann, Luigi Rumi, Peter Steurer, Willi Bannwarth, and Rolf Mülhaupt, *J. Am. Chem. Soc.* **131**, 8262 (2009)
- [26] Akbar Bagri, Cecilia Mattevi, Muge Acik, Yves J. Chabal, Manish Chhowalla, and Vivek B. Shenoy, *Nature Chem.* **2**, 581 (2010)
- [27] Jingzhi Shang, Lin Ma, Jiewei Li, Wei Ai, Ting Yu, and Gagik G. Gurzadyan, *Scientific Reports* **2**, 792 (2012)
- [28] Byung Hoon Kim, Soon-Young Oh, Hu Young Jeong, Han Young Yu, Yong Ju Yun, Yark Yeon Kim, Won G. Hong, Jeong Yong Lee, and Hae Jin Kim, *Appl. Phys. Lett.* **96**, 163111 (2010)
- [29] N. M. Martin, M. Van den Bossche, H. Grönbeck, C. Hakanoglu, F. Zhang, T. Li, J. Gustafson, J. F. Weaver, and E. Lundgren, *J. Phys. Chem C* **118**, 1118 (2013)
- [30] Hui-Lin Guo, Xian-Fei Wang, Qing-Yun Qian, Feng-Bin Wang, and Xing-Hua Xia, *ACS Nano* **3**, 2653 (2009)

[31] Vinayan Bhagavathi Parambath, Rupali Nagar, K. Sethupathi, and S. Ramaprabhu, *J. Phys. Chem C* **115**, 15679 (2011)

[32] Leila Shahriary, and Anjalía A. Athwale, *International Journal of Renewable Energy and Environmental Engineering* **2**, 58 (2014)

# Chapter 5

## Conclusion

Although many conduction mechanism of GO already reported, a comprehensive description on electrical conduction of multi-layered GO (MGO) was not enough. In this thesis, the effect of oxygen functional groups on the electrical transport of multi-layered graphene oxide was described. The oxygen functional groups were modulated by thermal annealing and H<sub>2</sub> gas pressure.

First, to investigate the electronic transport mechanisms in MGO, the temperature-dependent conductivity ( $\sigma(T)$ ) has been measured as a function of annealing temperature ( $T_a$ ). An individual MGO flake was gradually reduced by thermal annealing at temperatures  $T_a$  from 88 to 300 °C, reduction process of MGO flake upon heating is confirmed by X-ray photoelectron spectroscopy at each annealing stage. As  $T_a$  increases,  $\sigma(T)$  of the MGO increases. Unlike in a monolayer GO, the VRH model was not enough to describe the electrical transport of the reduced MGO. The VRH model in series with activation over small energy barriers was appropriate to explain the electrical transport of a reduced MGO. In other words, the  $\sigma(T)$  was well interpreted by variable-

range hopping in disordered regions in series with activated conduction across small barriers. The charge localized states were formed for hopping with the oxygen functional groups in GO, and the small activation barriers with the domain boundaries between the clustered oxygen functional groups and graphitic region. Since the increase of MGO graphitic domain area with an increase of  $T_a$  indicates an increase of the localization length in the VRH, the resistivity decreases at high temperatures. Both the hopping and activation barrier resistances decrease systematically as the  $T_a$  increases. At low temperatures, an additional activated resistivity is observed (in series with the VRH resistivity) and ascribed to the domain boundary in samples.

Secondly, MGO and PdGO were electrically evaluated for adsorptive hydrogen pressure at room temperature. PdGO was made by Suzuki-Miyaura coupling reaction using the MGO and Pd acetate, and dispersed Pd nanoparticles are confirmed by high resolution TEM. A pressure-dependent electrical conductance ( $G$ ) of MGO and PdGO has been measured during H<sub>2</sub> gas exposure (up to 20 bar) and release process. As the H<sub>2</sub> gas pressure increases, the  $G$  of MGO also increases while it decreases in PdGO. To elucidate the interaction between high pressure hydrogen molecules and PdGO, the states of MGO and PdGO before and after hydrogen exposure were investigated through AFM, HRTEM, XPS, and FT-IR analysis. In MGO, the oxygen functional group desorption occurs that is similar to the annealing

effect. Meanwhile, the hydrogen molecules are chemisorbed on dispersed Pd nanoparticles and dissociated in PdGO and the dissociated hydrogen atoms interact with PdO and form OH groups. The OH groups combine with carbon in PdGO and produce C-OH bonds. As a result, the  $G$  of PdGO decreases due to the decreased C/O ratio and more oxidized states induced by C-OH bonds. The  $G$  of the Pd particles themselves may also be affected by a hydrogen uptake. The PdGO oxidation explained by a hydrogen spillover effect and the decrease of electrical conductance may be due to this behavior.

## Publication list

[1] Seung Jae Baek, Won G. Hong, Min Park, Hae Jin Kim, Byung Hoon Kim, and Yung Woo Park, "Effect of Hydrogen Dissociation on the Electrical Conduction in Palladium-decorated Multi-layered Graphene Oxide", *Synth. Met.* **199**, 74-78 (2015)

[2] Seung Jae Baek, Won G. Hong, Min Park, Alan B. Kaiser, Hae Jin Kim, Byung Hoon Kim and Yung Woo Park, "The effect of oxygen functional groups on the electrical transport behavior of a single piece multi-layered graphene oxide", *Synth. Met.* **191**, 1-5 (2014)

[3] S. J. Hong, J. A. Rodríguez-Manzo, K. H. Kim, M. Park, S. J. Baek, D. I. Kholin, M. Lee, E. S. Choi, D. H. Jeong, D. A. Bonnell, E. J. Mele, M. Drndić, A. T. C. Johnson, and Y. W. Park, "Interlayer coupling measured by magnetoresistance (MR) in twisted bilayer graphene", *N. Journal of Physics in revision*.

[4] Byung Hoon Kim, Min Park, Minoh Lee, Seung Jae Baek, Hu Young Jung, Min Choi, Sung Jin Chang, Won G. Hong, Tae Kyung Kim, Hoi Ri Moon, Yung Woo Park, Noejung Park, and Yongseok Jun, "Effect of Sulfur Vacancy on Geometric and Electronic Structures of MoS<sub>2</sub> Induced by Molecular

Hydrogen Treatment at Room Temperature", *RSC Advances* **3**, 18424-18429 (2013)

[5] Young Soo Yun, Se Youn Cho, Jinyong Shim, Byung Hoon Kim, Sung-Jin Chang, Seung Jae Baek, Yun Suk Huh, Yongsug Tak, Yung Woo Park, Sungjin Park, and Hyoung-Joon Jin, "Microporous Carbon Nanoplates from Regenerated Silk Proteins for Supercapacitors", *Adv. Mater.* **25**, 1993-1998 (2013)

[6] Byung Hoon Kim, Sung Ju Hong, Seung Jae Baek, Hu Young Jeong, Noejung Park, Muyeong Lee, Sang Wook Lee, Min Park, Seung Wan Chu, Hyeon Suk Shin, Jeongmin Lim, Jeong Chul Lee, Yongseok Jun, and Yung Woo Park, "N-type graphene induced by dissociative H<sub>2</sub> adsorption at room temperature", *Scientific Reports* **2**, 690 (2012)

[7] Seung Wan Chu, Seung Jae Baek, Dong Chul Kim, Sunae Seo, Jun Sung Kim, and Yung Woo Park, "Charge transport in graphene doped with diatomic halogen molecules (I<sub>2</sub>, Br<sub>2</sub>) near Dirac point", *Synth. Met.* **162**, 1689-1693 (2012)

[8] Eui Yun Jang, Javier Carretero-González, Ajeong Choi, Wal Jun Kim, Mikhail E Kozlov, Taewoo Kim, Tae June Kang, Seung Jae Baek, Dae Weon Kim, Yung Woo Park, Ray H Baughman, and Yong Hyup Kim, "Fibers of reduced graphene oxide nanoribbons", *Nanotechnology* **23**, 235601 (2012)

- [9] Sejung Ahn, Yukyung Kim, Seungjae Baek, Shohei Ishimoto, Hideo Enozawa, Eigo Isomura, Masashi Hasegawa, Masahiko Iyoda and Yungwoo Park, "Synthesis and electrical conductivity of perchlorate-doped TTF-diamide nanofibers with double and triple helix structures", *J. Mater. Chem.* **20**, 10817-10823 (2010)
- [10] Eui Yun Jang, Tae June Kang, Hyeongwook Im, Seung Jae Baek, Seongyong Kim, Dae Hong Jeong, Yung Woo Park, and Yong Hyup Kim, "Macroscopic Single-Walled-Carbon-Nanotube Fiber Self-Assembled by Dip-Coating Method ", *Adv. Mat.* **21**, 1-5 (2009)
- [11] Johannes Svensson, Abdelrahim A. Sourab, Yury Tarakanov, Dong Su Lee, Seung Joo Park, Seung Jae Baek, Yung Woo Park, Eleanor E.B. Campbell, "Nanotube diameter dependence of the Schottky barrier height for Pd-carbon nanotube contacts ", *Nanotechnology* **20**, 175204 (2009)
- [12] B. H. Kim, T. H. Park, S. J. Baek, D. S. Lee, S. J. Park, J. S. Kim, Y. W. Park, "N-type carbon nanotube by alkaline-earth metal Sr doping ", *J. of Appl. Phys.* **103**, 096103 (2008)

## 요약 (국문초록)

그래핀에 대한 활발한 연구와는 별도로 산화그래핀에 대한 연구관심이 높아지고 있다. 초기에는 양질의 그래핀을 대량으로 합성하고자 하는 목적에서 시작하였다. 하지만 다양한 산소작용기를 지니고 있어 하이브리드가 용이하고 환원과정을 통해 전기전도성을 부여할 경우 에너지소자의 전극으로 활용이 가능하다는 등 여러분야의 응용 가능성을 보여주고 있어 산화그래핀 자체에도 많은 연구들이 이루어지고 있는 것이다. 특히 넓은 면적, 고르게 분산된 나노입자를 구속할 수 있다는 점에서 팔라듐(Pd)을 도핑한 산화그래핀은 수소연료전지의 전극으로의 활용이 기대되고 있다. 이에 따라 환원된 산화그래핀의 전기 전도 현상을 규명하기 위한 다양한 이론들이 제시되어 있지만 다결의 산화그래핀의 경우는 보고가 미비한 실정이다. 따라서 본 논문에서는 다결의 산화그래핀의 온도의존성 전기전도도 측정 및 Pd을 도핑한 다결 산화그래핀의 수소 압력의존성 전기전도도를 측정하여 다결의 산화그래핀에서 일어나는 전도 현상을 기술하고자 한다.

먼저 산화그래핀의 전기전도 특성을 파악하기 위하여 환원 온도에 따른 다결의 산화그래핀의 온도의존성 전기전도도를 측정하였다. 하나의 샘플에서 점진적으로 환원온도 (88, 158, 215, 250, 250, 300 °C)를 높여가며 진행하였으며 각 환원온도에서의 탄소/산소그룹 조성은 XPS를 통하여 확인되

었다. 그 결과, 환원온도가 높아질수록 산소작용기는 감소하게 되며 전기전도도는 증가함을 발견하였다. 전기전도 특성은 가변범위호핑 (Variable Range Hopping : VRH)과 직렬로 연결된 활성화된 전도(activated conduction)의 합으로 잘 설명되었다. 즉, 산화그래핀의 산소작용기 그룹의 도메인(domain) 안에서는 호핑을 위한 국소영역이 형성되어 VRH가 일어나고 도메인의 경계에는 작은 장벽이 형성되어 활성화된 전도가 일어나게 되는 것이다. 환원온도가 높아질수록 호핑 저항과 장벽 저항이 감소하였다.

그 다음으로 상온에서 다결 산화그래핀과 Pd이 도핑된 다결 산화그래핀의 고압의 수소 환경에서 수소 흡착에 따른 전기전도도 특성을 분석하였다. Pd이 도핑된 산화그래핀은 Suzuki-Miyaura coupling reaction을 사용하여 만들어졌으며 HRTEM을 통하여 Pd 나노입자가 고르게 분산되어 있음을 확인하였다. Pd이 도핑된 다결 산화그래핀의 수소 흡착 특성을 알아보기 위해 먼저 다결 산화그래핀을 절대온도 300도에서 20 bar 까지 수소압력을 높혀가며 수소압에 따른 전기전도도를 측정하였으며 그 후 Pd이 도핑된 산화그래핀도 같은 방법으로 실시하였다. 또한 다시 수소압을 감소시키며 측정을 하였고 진공상태로 만든 후 재측정을 실시하였다. 그 결과, 수소압이 증가할수록 다결 산화그래핀의 전기전도도는 증가하였으나 Pd이 도핑된 다결 산화그래핀은 감소하는 현상을 보였다. AFM, XPS, FT-IR 분석을 통하여 MGO의 전기전도도 증가

는 수소가스에 의한 MGO 환원이 원인일 것으로 여겨진다. 반면 PdGO에서는 수소가 해리되어 -OH 그룹이 형성됨과 PdO가 환원되었음을 발견하였다. 결과적으로 -OH 그룹의 생성은 PdGO를 더욱 산화시켜 전기전도도는 감소하게 된다.

주제어: 산화그래핀, 전하수송, 팔라듐도핑, 수소환경, X-선 광전자 분광법, 산소작용기

학번: 2009-30729